

# ~~Short Communication:~~ Evaluating the accuracy of binary classifiers for geomorphic applications

Matthew W. Rossi<sup>1</sup>

<sup>1</sup>Earth Lab, Cooperative Institute for Research in Environmental Sciences, The University of Colorado, Boulder, CO 80303, USA

Correspondence to: Matthew W. Rossi (matthew.rossi@colorado.edu)

**Abstract.** ~~Airborne lidar~~ Increased access to high resolution topography has revolutionized our ability to map out fine-scale (~~-1 m~~) topographic features at watershed- to landscape-scales. As our ‘vision’ of land surface has improved, so has ~~our~~ the need for more robust quantification of the accuracy of the geomorphic maps we derive from these data. One broad class of mapping challenges is that of binary classification where remote sensing data are used to identify the presence or absence of a given feature. Fortunately, there are a large suite of metrics developed in the data sciences that are well suited to quantifying pixel-level accuracy of binary classifiers. ~~In this paper, I focus on the challenge of identifying bedrock from lidar topography, though the insights gleaned from this analysis apply to any task where~~ This analysis focuses on how these metrics perform when there is a need to quantify how the number and extent of landforms are expected to vary as a function of the environmental forcing. ~~Using (e.g., due to climate, ecology, material property, erosion rate). Results from~~ a suite of synthetic ~~maps, surfaces~~ show how the most widely used pixel-level accuracy metric, *F1-score*, is particularly poorly suited to quantifying accuracy for this kind of application. Well-known biases to imbalanced data are exacerbated by methodological strategies that ~~attempt to~~ calibrate and validate classifiers across ~~a range of geomorphic~~ settings where feature abundances vary. *Matthews Correlation Coefficient* largely removes this bias over a wide range of feature abundances, such that the sensitivity of accuracy scores to geomorphic setting instead embeds information about the ~~error structure of the classification. To this end, I examine how the scale size and shape of features (e.g., the typical sizes of bedrock outcrops) and the type of error. If error (e.g., is random versus systematic) manifest in pixel-level scores. The normalized version of~~ Matthews Correlation Coefficient is relatively insensitive to feature ~~scale if error is random and if large enough areas are mapped. In contrast, a size and shape, though preferential modification of the dominant class can limit the domain over which scores can be compared. If the error is systematic (e.g., due to co-registration error between remote sensing datasets), this metric shows strong sensitivity to feature size and shape emerges when classifier error is systematic. My findings highlight the importance of choosing appropriate pixel levels such that smaller features with more complex boundaries induce more classification error. Future studies should build on this analysis by interrogating how pixel-level accuracy metrics when evaluating topographic surfaces where respond to different kinds of feature abundances strongly vary. It is necessary to understand how pixel-level metrics are expected to perform as a function of scene-level properties before interpreting empirical observations. distributions indicative of different types of surface processes.~~



# 1 Motivation

35 ~~The increasing acquisition and access to lidar topography has revolutionized~~High resolution topographic datasets are transforming our ability to characterize the fine-scale structure of the Earth's surface (Roering et al., 2013; Passalacqua et al., 2015). ~~Because lidar can 'see' through the forest canopy, this technical advance enables quantification of~~Airborne lidar especially, has changed how geomorphic fieldwork is conducted by enabling scientists to quantify the form and extent of meter-scale features over large areas ~~when mounted on an airborne platform. Detailed mapping of such features is invaluable to~~(Roering et al., 2013). ~~Because lidar 'sees' through vegetation, lidar has accelerated progress in~~ both discovery science and 40 testing hypotheses where the prevalence of features is expected to vary as a function of the environmental forcing (e.g., in response to ~~changesdifferences~~ in climate, ~~ecosystem, rock properties, uplift rates~~). For example, ~~airborne lidar ecology, material property, erosion rate~~. Airborne lidar has now been used to map ~~termite mounds (Levick et al., 2010),~~mima mounds (Reed & Amundson, 2012), ~~termite mounds (Levick et al., 2010; Davies et al., 2014), ,~~ tree throw pits and mounds (Roering et al., 2010; Doane et al., ~~20212023~~), landslide boundaries and classes (Jaboyedoff et al, 2012; ~~Bunn et al., 2019;~~ Prakesh et al., 2020), channel ~~network and channel head locations networks~~ (Pirotti & Tarolli, 2010; Clubb et al., ~~2014,~~ ~~exposed bedrock (DiBiase et al., 2012; Marshall and Roering, 2014; MilodowskiKorzeniowska et al., 2015), and2018),~~ bedrock structure and ~~faulting~~ (Cunningham et al., 2006; Pavlis and Bruhn, 2011; Morell et al., 2017), ~~), and bedrock exposure (DiBiase et al., 2012; Milodowski et al., 2015; Rossi et al., 2020).~~

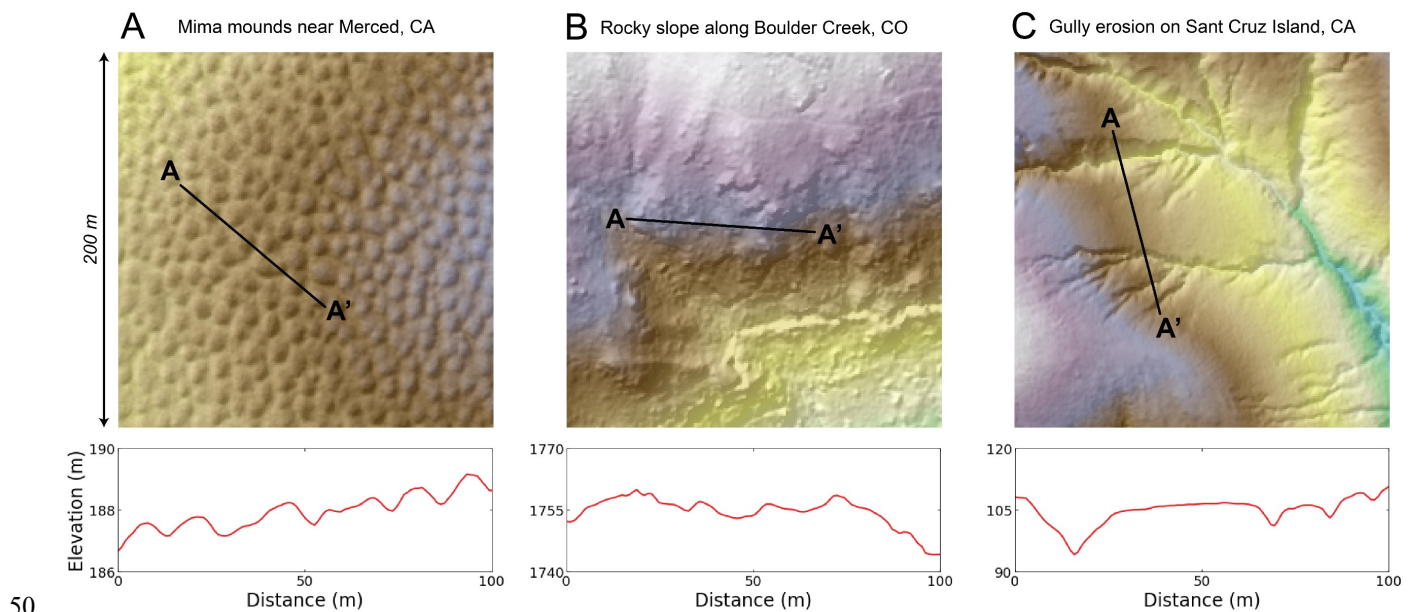


**Figure 1:** (A) Mima mounds near Merced, CA, USA, (B) bedrock outcrops along Boulder Creek, CO, USA, and (C) gully erosion on Santa Cruz Island, CA, USA as observed from 1-m shaded relief maps. Note that even though the areal extent is the same among these scenes (200 x 200 m), topographic relief is drastically different (total relief in A is 7 m, in B is 146 m, and in C is 76 m). 100-m elevation transects from A to A' for each site are shown to illustrate how different features manifest as roughness elements in the topography. Airborne lidar for the

55 mima mound and rocky slope sites was flown by the National Center for Airborne Laser Mapping (NCALM). Airborne lidar for the gully erosion site was flown by the United States Geological Survey (USGS). All lidar datasets were downloaded from OpenTopography (Reed, 2006; Anderson et al., 2011; 2010 Channel Islands Lidar Collection, 2012). Interpretations of features classified from lidar data can be found in Reed & Amundson (2011), Rossi et al. (2020), and Korzeniowska et al. (2018) for the mima mound, rocky slope, and gully sites, respectively.

60 Figure 1 shows three examples of features that can be mapped using 1-m airborne lidar data. The utility of lidar topography to binary classification of feature locations for each of these geomorphic applications is unquestioned. These clear. However, examples also highlight that one of the most common uses for lidar topography is for large-scale features. However, the number, size, shape, amplitude, and pattern of features can vary. Regular, repeating morphologies with a characteristic spatial scale, binary classification of finer-scale features. While (e.g., mima mounds in Fig. 1A; Reed and Amundson, 2011) pose different challenges to classification than irregular, heterogeneous morphologies that occur at many scales (e.g., bedrock exposure in Fig. 1B; Rossi et al., 2020). Furthermore, the importance of flowing water on surface processes means that many geomorphic features form directional networks with substantial anisotropy (e.g., gully erosion in Fig. 1C; Korzeniowska et al., 2018). Perhaps unsurprisingly then, accuracy assessment in the geomorphic literature has varied a lot even as formal methods for

65 evaluating pixel-level accuracy of binary classifiers isare now becoming standard practice in the remote sensing and machine learning literature (e.g., Wang et al., 2019; Prakesh et al., 2020; Agren et al, 2021),-. Slow adoption of these standard methods in accuracy assessment in the geomorphic literature is quite variable. This is likely due to may arise from two tendencies of geomorphic studies that employ lidar classifiers: 1. Process-based studies are typically more interested in the properties and densities of features rather than their contingent locations; 2. Classifiers are expected to work across large gradients in the prevalence of features to test our understanding of the relevant transport laws at play. The former tendency arises from the fact that predicting the actual locations of features (e.g., mounds, outcrops, mounds, channels) is not typically usually a viable target for numerical models of landscapes where uncertainty in initial conditions and the stochastic nature of processes preclude a deterministic forecasting of surface evolution. finer-scale locations of features (e.g., Barnhart et al., 2020). The latter tendency arises from the need to use classified data to constrain natural experiments where geomorphic transport laws (Dietrich et al.,

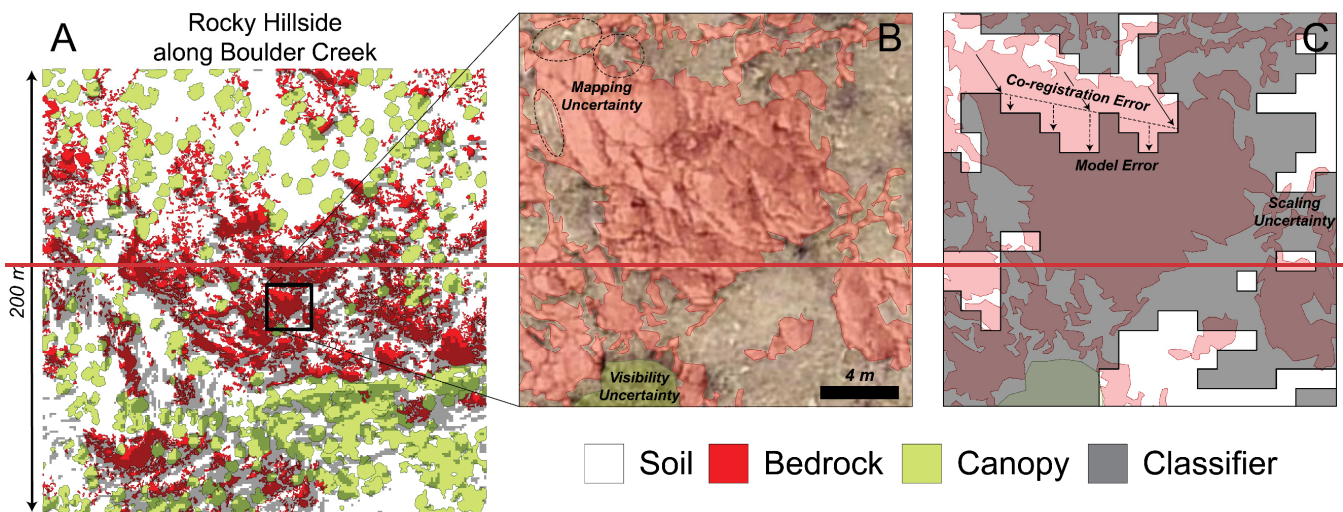
70 2003) can be tested against governing variables (e.g., across climo-, eco-, litho-, or tectono-sequences). I showAs shown below that, these tendencies can be at odds with pixel-level accuracy metrics that are designed to assess positional accuracy for similarly-balanced data (i.e., data where the frequency of positive and negative values does not dramatically vary from case to caseare similar).

85 ThereNevertheless, there are several important benefits to adopting pixel-level accuracy metrics when reporting the success of geomorphic classifiers. First, these metrics provide common standards for evaluating classifier accuracy across studies, including direct comparison between proxy-based classifiers withand those developed using machine learning. Second, trends in pixel-level accuracy scores may reveal distinct patterns in the spatial structure of error. Third, pixel-level measures are easy to apply to new objectives as long as their limitations are properly considered. To this end, I focusThis paper focuses on how

90 two widely used metrics, *F-measures* (van Rijsbergen, 1979, 1974; Chinchor, 1992) and *Matthews Correlation Coefficient* (Matthews, 1975; Baldi et al., 2000), perform when the research design intentionally calibrates and tests binary classifiers across large gradients in how balanced the data are. Interactions among feature size, feature shape, and error structure can produce diagnostic trends in accuracy scores as a function of feature prevalence. As such, I argue here that pixel-level accuracy scores should be evaluated alongside performance at other scales, particularly the scene level scale where the statistical attributes of features can be quantified for a given environmental forcing. The general approach is to synthetically generate 'model' and 'truth' data that have a known error structure. Pixel-level accuracy scores are then calculated as a function of feature abundance. Despite the simplicity of the scenarios considered, this analysis helps constrain the range over which pixel-level metrics can be reliably compared across gradients in feature abundance. Synthetic scenarios also reveal how the shape and scale of individual objects can strongly influence pixel-level scores when there are small co-registration errors between

95

100 model and truth data.



105 **Figure 1:** Example bedrock mapping from Rossi et al. (2020) showing (A) a classified scene. Zoom boxes illustrate different kinds of error due to (B) mapping 'truth' from air photos and (C) using coarser resolution lidar data to 'model' bedrock. In A, scene-level patterns in actual bedrock exposure were mapped using 3-inch Pictometry® air photos and a topographic proxy derived from 1-m airborne lidar (Anderson et al., 2012) as the classifier. The bedrock fraction mapped from air photos is 0.24. The bedrock fraction mapped from lidar data using a regionally based, slope threshold of  $38^\circ$  is 0.35. The zoom area used for B and C is shown in A as a black box. In B, the truth map for this site is overlaid on associated air photos at 75% transparency to show the two principal sources of error in air photo mapping. In C, the bedrock classifier is overlaid on the same truth map to show the three principal sources of error in using the lidar data for classification.

110

## 2 Example application: Bedrock mapping

The task of mapping bedrock outcrops is useful to show how pixel-level accuracy metrics can be applied to geomorphic studies for a few reasons. First, the transition from fully soil-mantled to bedrock-dominated hillsides reflects an important continuum

in process dominance and rates (Heimsath et al., 2012). Whether and where bedrock is observed records the local (im)balance  
115 between soil production and denudation rates (Gilbert, 1909), providing important tests to hypothesized soil production  
functions (e.g., exponential versus ‘humped’; Heimsath et al., 1997; Anderson, 2002) and sediment transport laws (e.g., linear  
versus nonlinear creep; Culling, 1963; Andrews & Bucknam, 1987). Second, the challenge of mapping bedrock using airborne  
lidar data is an application that has received a fair bit of recent attention (DiBiase et al., 2012; Marshall & Roering, 2014;  
Milodowski et al., 2015; Rossi et al., 2020). This is, in part, because individual bedrock features can be resolved in lidar  
120 topography using physically interpretable slope and roughness thresholds. Airborne lidar balances trade-offs between data  
resolution (~1 m) and data coverage (100’s of km<sup>2</sup>) and thus is well suited to exploring how feature density and properties  
vary across environmental gradients. Third, identifying bedrock typifies the more general challenge of understanding the  
related, but distinct, scaling properties among data, features, and processes (Sofia, 2020). Bedrock tors and cliffs occur at many  
scales (sub-meter to tens of meters) that reside on hillsides (hundreds of meters in length) which are, in turn, responding to  
125 base-level signals propagating through river networks (tens to thousands of km<sup>2</sup>).

In this paper, I specifically consider the approach taken by DiBiase et al. (2012) and adopted by Rossi et al. (2020). These  
studies calibrated lidar proxies for bedrock in the San Gabriel Mountains, CA, USA (SGM) and the Colorado Front Range,  
CO, USA (CFR), respectively. The general approach in both was to map bedrock using photographic imagery for 50 x 50 m  
130 to 200 x 200 m patches where the ground surface is visible due to limited forest cover and/or recent clearing due to wildfire.  
By selecting scenes representative of a large range of bedrock fractions, the main goal of these studies was to identify a single  
slope threshold that could be applied across the landscape. Both studies found strongest correlations using slope thresholds  
somewhat above the angle of repose for granular materials (45° in the SGM and 43° in CFR). However, the threshold that  
most closely reproduced the scene level bedrock fraction without rescaling is closer to expected values for the angle of repose  
135 (e.g., a slope threshold of 38° produced a regression slope of one in the CFR; Rossi et al., 2020). Regressions in the CFR were  
overall weaker, likely due to differences in air photo mapping (1–10 cm surface normal field photos in the SGM versus ~8 cm  
air photos in the CFR) and the increased prevalence of bedrock tors, or isolated bedrock outcrops within a lower relief soil  
mantle. Bedrock tors tend to produce dome-shaped features with steep slopes on their sides and low-sloped tops that may be  
better resolved using roughness-based topographic proxies (Milodowski et al., 2015). While scene-level success of slope-based  
140 proxies for bedrock in the SGM (peak  $r^2$  of 0.99) and CFR (peak  $r^2$  of 0.85) are promising, neither study assessed pixel-level  
accuracy.

Figure 1 shows two general challenges associated with using air photos to calibrate and validate lidar-based proxies for bedrock  
exposure. The first general source of error is introduced in the generation of ‘truth’ data from air photos (Fig. 1B). Even under  
145 the best circumstances, **visibility** of the ground surface is obstructed in places by the vegetation canopy. This can be partially  
addressed by restricting mapping tasks to areas where obstructions are minimal and ground truthing air photo mapping with  
field observations. While using high-resolution air photos aids interpretation, it is difficult to fully eliminate human error in

**mapping** due to shadows or weakly contrasting visible properties between bedrock and soil. Similarly, distinguishing in-place bedrock from detached coarse sediment is difficult unless coarse sediment collects into macro-scale features, like talus slopes, whose properties are distinct. The second general source of error arises in the classification process itself (Fig. 1C). Relating higher resolution air photos to lidar proxies requires better understanding of uncertainty in the **scaling** properties of features. Scaling challenges arise from both the feature shape itself and how gridded representations of features change as a function of data resolution. Because the classifier is often built from data acquired at different times and using different data sources, error in classification can also arise due to **co-registration** of truth and model datasets. Precise mapping of control points for georeferencing and smart use of stable surfaces in post-processing can help minimize the misfit between truth and model data (Bertin et al, 2022). The binary classifier itself, whether using physical thresholds or statistical models, will also be imperfect. New algorithms attempt to make this **model** error as small as possible. Each of these five sources of error lies on a continuum between random and systematic, where random error is independent of feature locations or properties and systematic error refers to any error structure that is spatially correlated with feature locations or properties. For example, we might expect co-registration error between two remote sensing datasets to be more systematic than the others due to translation, rotation, and distortion of aligned datasets. Can pixel-level accuracy scores diagnose different error structures when calibration of binary classifiers is attempted against scenes that span large gradients in bedrock exposure? How does feature shape, feature scale, and mapping coverage interact with this error structure?

### 3 Approach

Two of the most widely used accuracy metrics are *F1 score* and *Matthews Correlation Coefficient (MCC)*. Adopting such pixel-level metrics helps link studies that classify features using physical intuition (e.g., using slope thresholds for bedrock exposure is based on the notion that only bedrock is stable above the angle of repose) with those developed using statistical methods (e.g., machine learning). These measures also provide a common language to assess results from studies that span different landscapes with different research goals. However, I emphasize here that while these metrics can robustly characterize pixel-level accuracy, it is important to consider their limitations in characterizing scene-level accuracy and how they might perform across gradients in environmental forcing. To this end, I consider a suite of synthetic land surfaces that show the sensitivity of *F1 score* and a normalized version of *MCC* to: feature scale, the error structure in the data, and how balanced the data are. In Section 3, I describe methods common to all scenarios. Specifically, I describe the general process of generating grids and calculating accuracy scores. Methods unique to each different scenario are then described in Sections 4 and 5 so that their rationale can be articulated in the context of results.

### 3.2 Approach

One common use of binary classifiers is to build an inventory of feature boundaries and abundances using remotely sensed data. This typically entails using scenes where ‘truth’ is known through detailed field or air photo mapping. An algorithm built from an independent data source (e.g., lidar) is then used to ‘model’ the locations of features. Models are commonly trained and tested so that the classifier can be used for larger scale geomorphic mapping. If the density, size distribution, and form of features varies from scene to scene, then it is important to understand how pixel-level accuracy metrics will perform as a function of scene-level properties (e.g., feature fraction). To mimic this task, this paper examines how two widely used accuracy metrics, *F1-score* and *Matthews Correlation Coefficient (MCC)*, behave on synthetic truth and model data. Synthetic truth data is generated by randomly placing features in a scene at a given abundance. Model data is either independent from truth data or derived from the truth data using an assumed error structure. Pixel-level accuracy scores are then calculated for each scene.

#### 2.1 Grid generation

To generate ‘truth’ grids of ~~bedrock and soil~~, I first use features within a matrix, the pseudo-random number generator in NumPy is used to create a scene of size  $m \times n$  cells. Continuous values are converted into binary classes (0 = ~~soil~~matrix; 1 = ~~bedrock~~feature) based on a user-specified value for the ~~overall~~feature fraction of ~~bedrock~~ ( $f_B - f_f$ ), which is simply the fraction of the surface covered by features. The simplest scenario is for ~~bedrock~~ ~~to~~ ~~rs~~features with a size of one pixel. While synthetic surfaces are scale free, I ~~report~~ results ~~are reported~~ assuming a grid spacing of 1-m to represent a typical case using airborne lidar. To simulate features that have a scale greater than one square meter, I ~~use~~ the pseudo-random numbers ~~to~~ instead specify a first guess at the locations of the centres of ~~to~~ ~~rs~~features. The first guess at the number of ~~to~~ ~~rs~~features is calculated by finding the integer number of ~~to~~ ~~rs~~features of length,  $l$ , that most closely matches  $f_B f_f$ . However, as the number of ~~to~~ ~~rs~~feature centres increases, so does the probability that two neighbouring ~~to~~ ~~rs~~objects overlap and coalesce into a larger ~~feature~~object. As such, the first guess generally produces an actual ~~bedrock~~feature fraction lower than the user-specified value. The ratio between the specified  $f_B f_f$  and this underestimate is then used to proportionally increase the number of incipient ~~to~~ ~~rs~~features in the model domain. I ~~iterate this~~ The process is iterated until either the synthetic fraction is within 0.5% of the specified value or fifty iterations, whichever comes first. It is worth pointing out here that while I will continue to use the term ‘~~to~~ ~~rs~~ density’ to refer to the ~~The~~ number of ~~to~~ ~~rs~~centres per scene area, the resultant incipient objects is always higher than the actual number of ~~to~~ ~~rs~~isobjects in the scene because smaller ~~due to the coalescing of~~ incipient features (see section 6.2 and Appendix B2 for further elaboration) increasingly coalesce into larger objects at higher feature fractions.

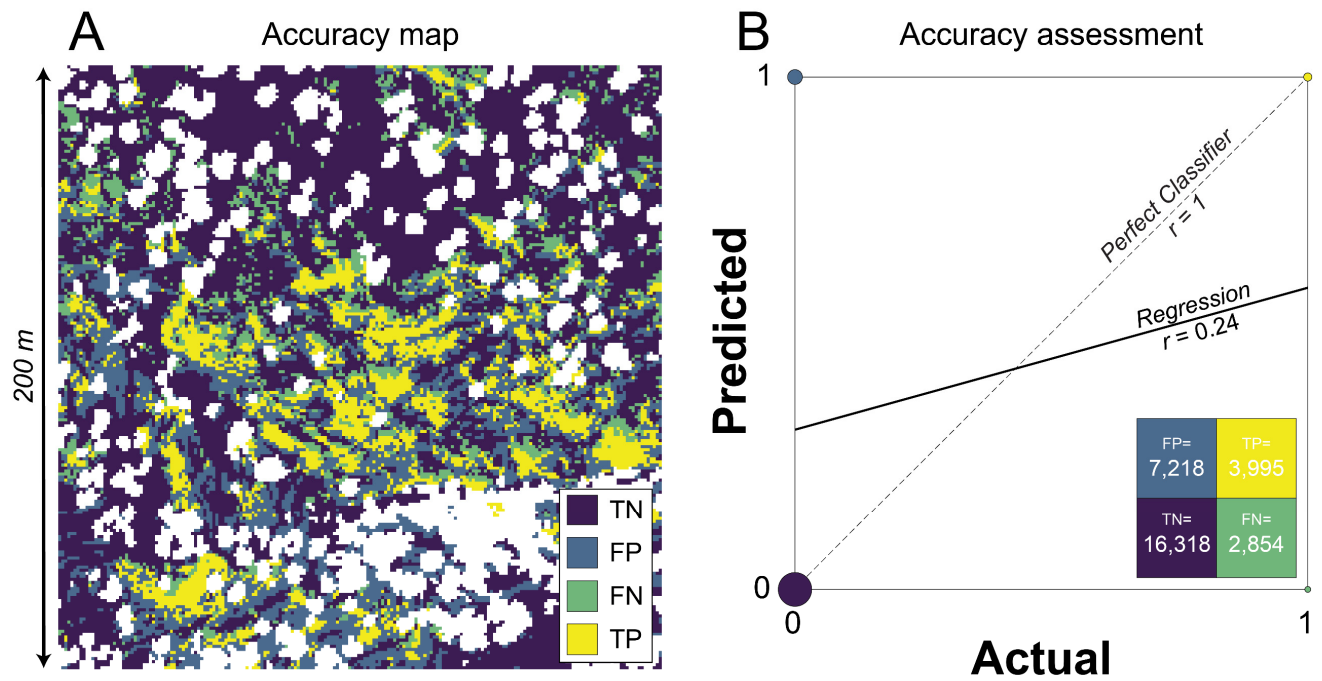
All scenarios ~~presented~~ in this study rely on comparing simulated ‘truth’ and ‘model’ grids ~~across the full range of feature fractions ( $0 < f_f < 1$ )~~. Where the truth and model data are independent of each other, the two grids are generated using different pseudo-random seed numbers in NumPy (section 4.3). In scenarios where the model grid is dependent on the truth grid, the



model grid is a copy of the truth data using the specified error structure. Details for how random error (section 54.1), systematic error (section 54.2), and random plus systematic error (section 54.3) are implemented are described in context below. For each scenario, the truth and model grids are evaluated by building the confusion matrix and calculating accuracy metrics at each ~~bedrock~~feature fraction (section 32.2).

### 32.2 Pixel-level accuracy metrics

While there are many metrics used to quantify the accuracy of binary classifiers, ~~the focus hereof this paper is~~ on two of the ~~most~~ widely used ones: the *F1-score* and *Matthews Correlation Coefficient (MCC)*. These metrics ~~can be~~ frequently used to evaluate pixel-level performance of classified maps ~~with respect to ground truth data and are often used when employing generated from~~ machine learning techniques (e.g., Wang et al., 2019; Prakesh et al., 2020; Agren et al., 2021). Application of these metrics need not be limited to the training and testing of machine learning algorithms. They are broadly useful to any binary classification task where positional accuracy is important. Both *F1-score* and *MCC* can be calculated directly from the confusion matrix. The confusion matrix for binary classification is a 2x2 table where the column headers are the true classes and the row headers are the model classes, thereby summarizing the occurrence of the four possible classification outcomes: True Negatives (TN), True Positives (TP), False Positives (FP), and False Negatives (FN).



225 **Figure 2:** (A) Pixel classes for Fig. 1B and (B) the corresponding confusion matrix (inset) and correlation plot (main). In A, the four outcomes of the binary classification are shown in colour [TN = True Negatives; FP = False Positives; FN = False Negatives; TP = True Positives]. The areas in white were obscured by the vegetation canopy in air photos (24% of area) and thus excluded from accuracy assessment. In B, the colours of each cell in the confusion matrix and each point in the plot are the same as in A. The number of observations for each class is shown in the confusion matrix and point sizes on the plot are scaled to the relative frequency of each value. This classified map is site P01 from Rossi et al. (2020), where more details on mapping methods are described.

230 For example, the example scene in Figure 1A can be B is readily reclassified into these four outcomes (Fig. 2A) ~~which 2A~~  
 using the feature mapping from Rossi et al. (2020). The frequency of these outcomes is summarized by using the confusion  
 matrix ~~shown in the inset of Figure (Fig. 2B: inset)~~. The simplest ~~assessment of~~ accuracy metric is the overall accuracy (OA),  
 and its complement the error rate (ER), where:

$$OA = \frac{TP+TN}{TP+TN+FP+FN} \quad (1)$$

235 
$$ER = \frac{FP+FN}{TP+TN+FP+FN} \quad (2)$$

While *OA* and *ER* are straightforward to calculate, they provide little insight into the relative frequencies of FP and FN. To  
 address this limitation, there are a large family of accuracy metrics that better characterize different types of error. For example,  
*precision* and *recall* characterize the relative frequencies of FP and FN explicitly. *Precision*, also known as the positive  
 predictive value, is the ratio of true positives to all positives predicted by the model (accounts for FP) ~~and recall~~:

240 
$$\text{Precision} = \frac{TP}{TP+FP} \quad (3)$$

*Recall*, also known as the true positive rate, is the ratio of true positives to all positives (accounts for FN) ~~whereby~~:

$$\text{Precision} = \frac{TP}{TP+FP} \quad (3)$$

$$\text{Recall} = \frac{TP}{TP+FN} \quad (4)$$

Figure 2 is an example where the *precision* is low (0.36), but the *recall* is reasonably good (0.58) (Table 1). *F-measures* were  
 245 designed to summarize *precision* and *recall* into a single metric (van Rijsbergen, 1979; Chinchor, 1992). The case where  
 both are equally weighted is referred to as the *F1-score*, where:

$$F1\text{-score} = \frac{2 \times TP}{(2 \times TP) + FP + FN} \quad (5)$$

By representing the harmonic mean of *precision* and *recall*, this metric accounts for both errors of omission and commission.  
 However, *F1-scores* only characterize the success at identifying the target class, and low values can occur even if the overall  
 250 accuracy is high because it excludes True Negatives. ~~Consequently~~ As such, this metric is quite sensitive to the prevalence of  
 positive values ~~whereby higher~~. Higher *F1-scores* are favoured when the positive class is more abundant (e.g., Chicco and  
 Jurman, 2020). Related to this sensitivity to imbalanced data is the property of asymmetry. Asymmetric metrics are those  
 where the accuracy score differs when the target classes are switched. Table 1 shows that the *F1-score* for Figure 2 would be  
 72% higher if the target class/feature was soil instead of bedrock. Asymmetry arises because there is more soil than bedrock in  
 255 the scene and TN are not included in calculations of *precision*, *recall*, or *F1-score*. These well-known limitations of *F-measures*  
 are better handled by metrics that incorporate all four classes of the confusion matrix. One such metric is *Matthews Correlation  
 Coefficient (MCC)*, where:

$$MCC = \frac{(TP \times TN) - (FP \times FN)}{\sqrt{(TP+FP) \times (TP+FN) \times (TN+FP) \times (TN+FN)}} \quad (6)$$

260  $MCC$  is equivalent to a Pearson’s correlation coefficient where the model classes are regressed against the true classes in a binary classification task (Fig. 2B). Values of  $MCC$  can be similarly interpreted where -1.0 indicates perfect anti-correlation, 0 is a random model, and 1.0 indicates perfect correlation. And while  $MCC$  is just one of several metrics that include all four quadrants of the confusion matrix (e.g., Balanced Accuracy, Markedness, Cohen’s Kappa), [recent work suggests that  \$MCC\$  appears to be](#) the most robust to imbalanced data (Chicco and Jurman, 2020; Chicco et al., 2021a; Chicco et al., 2021b). In this analysis, I report ~~the~~ normalized version of  $MCC$  as:

265 
$$nMCC = \frac{MCC+1}{2} \quad (7)$$

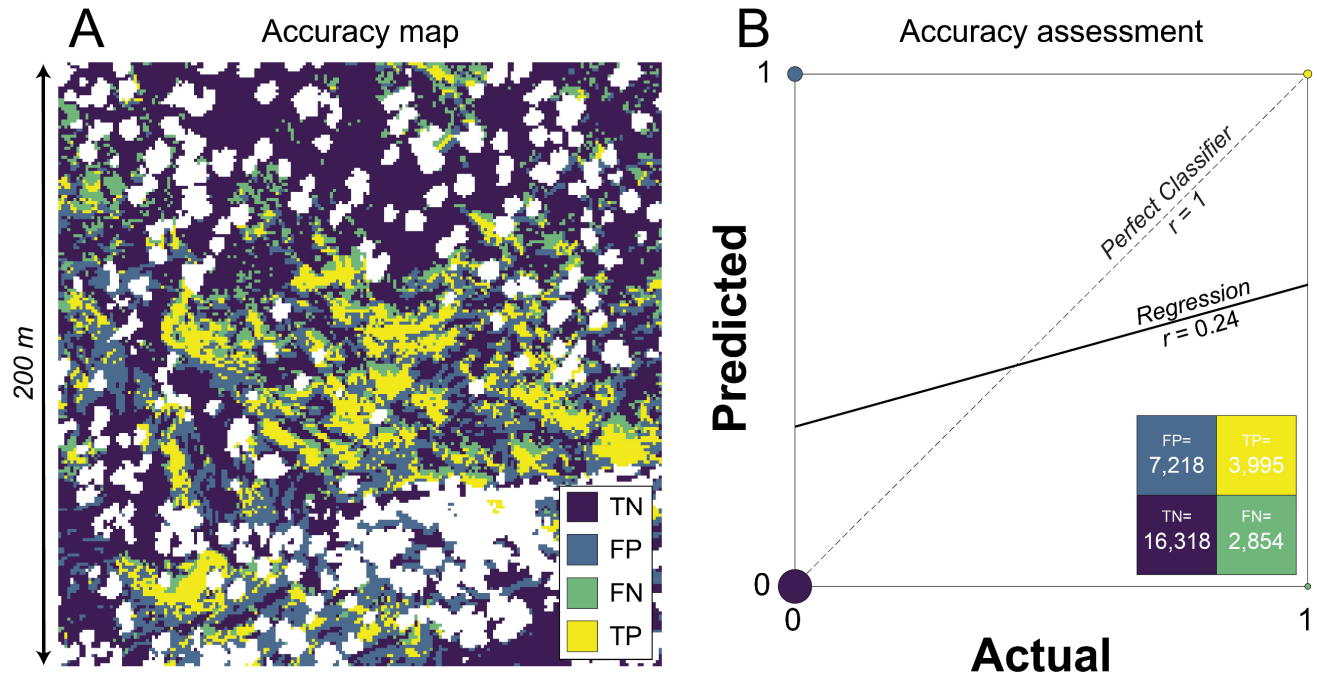
By re-scaling  $MCC$  from zero to one,  $nMCC$  facilitates comparison with  $F1$ -score on plots and in discussion. It is worth noting [here](#) though that interpretations of low values of  $nMCC$  differ from interpretations of low values of  $F1$ -score. The former implies anti-correlation between model and truth data while the latter does not. For example, the scene in Figure 2 indicates a weak positive correlation (i.e.,  $nMCC$  greater than 0.5) even though the  $F1$ -score is lower than 0.5 (Table 1). As such, direct comparison of these metrics should be done with caution.

270

**Table 1:** Accuracy metrics for Figure 2 using the alternative target classes of bedrock and soil.

Target Class	$OA^*$	$ER^*$	$Precision$	$Recall$	$F1$ -score	$MCC^*$	$nMCC^*$
<del>Bedrock</del> Feature (bedrock)	0.67	0.33	0.36	0.58	0.44	0.24	0.62
SoilFeature (soil)	0.67	0.33	0.85	0.69	0.76	0.24	0.62

\* Metrics that do not vary as a function of the target class in binary classification.



280 **Figure 2:** (A) Pixel classes for Fig. 1A and (B) the corresponding confusion matrix (inset) and correlation plot (main). In A, the four outcomes of the binary classification are shown in colour [TN = True Negatives; FP = False Positives; FN = False Negatives; TP = True Positives]. The areas in white were obscured by the vegetation canopy in air photos (24% of area) and thus excluded from accuracy assessment. In B, the colours of each cell in the confusion matrix and each point in the plot are the same as in A. The number of observations for each class is shown in the confusion matrix and point sizes on the plot are scaled to the relative frequency of each value.

#### 4 Pixel level versus scene level accuracy

285 Throughout this analysis, I distinguish between pixel-level and scene-level measures of accuracy, in part, motivates the approach taken to examine how accuracy metrics handle imbalanced data in this study. Pixel-level accuracy requires that the precise locations of features are honoured where the, with a lower bound to feature detection is set by the spatial resolution of the data used. Scene-level accuracy characterizes the mismatch between model and truth data at some coarser scale and typically assesses statistical properties of the target feature class (e.g., bedrock fraction, mound densities, drainage densities). While high pixel-level accuracy ensures high scene-level accuracy, the converse need not be true. This distinction is motivated by studies where calibration of lidar classifiers was undertaken only at the scene level (DiBiase et al., 2012; Rossi et al., 2020) and whose rationale was summarized in section 2. Scene level assessment alone may lead to different findings than pixel level assessment. For example, a related effort by Milodowski et al. (2015) showed that lidar based, roughness thresholds provide an alternative topographic proxy that can be more successful than slope based ones in some landscapes. While their overall objective of finding a classifier that worked across a range of bedrock fractions was similar to DiBiase et al. (2012), these

295 ~~authors used pixel-level assessment to select thresholds and evaluate classifier success. As such, there is a need to understand~~  
~~how pixel-level assessments behave when classifying data where scenes are intentionally selected across gradients in how~~  
~~balanced the data are.~~Given the importance of developing binary classifiers that work across a range of feature densities and  
sizes, there is a need to better understand how pixel-level accuracy metrics perform across a range of scene-level properties  
like feature fraction. One mark of a good accuracy metric is its ability to diagnose the case of independence. In this context,  
300 independence means that the locations of features in the model contain no information about the true locations of features. If  
accuracy metrics produce similar scores when the model and truth data are independent from each other, then it means the  
metric can be reliably compared for different feature fractions. A perhaps trivial example is the case where feature fractions  
are assumed to be constant (e.g., total feature coverage) regardless of the true feature fraction. A more interesting example is  
the case where scene-level fractions are the same in the truth and model data (i.e., high scene-level accuracy) but where the  
305 actual locations of features are unrelated (i.e., low pixel-level accuracy).

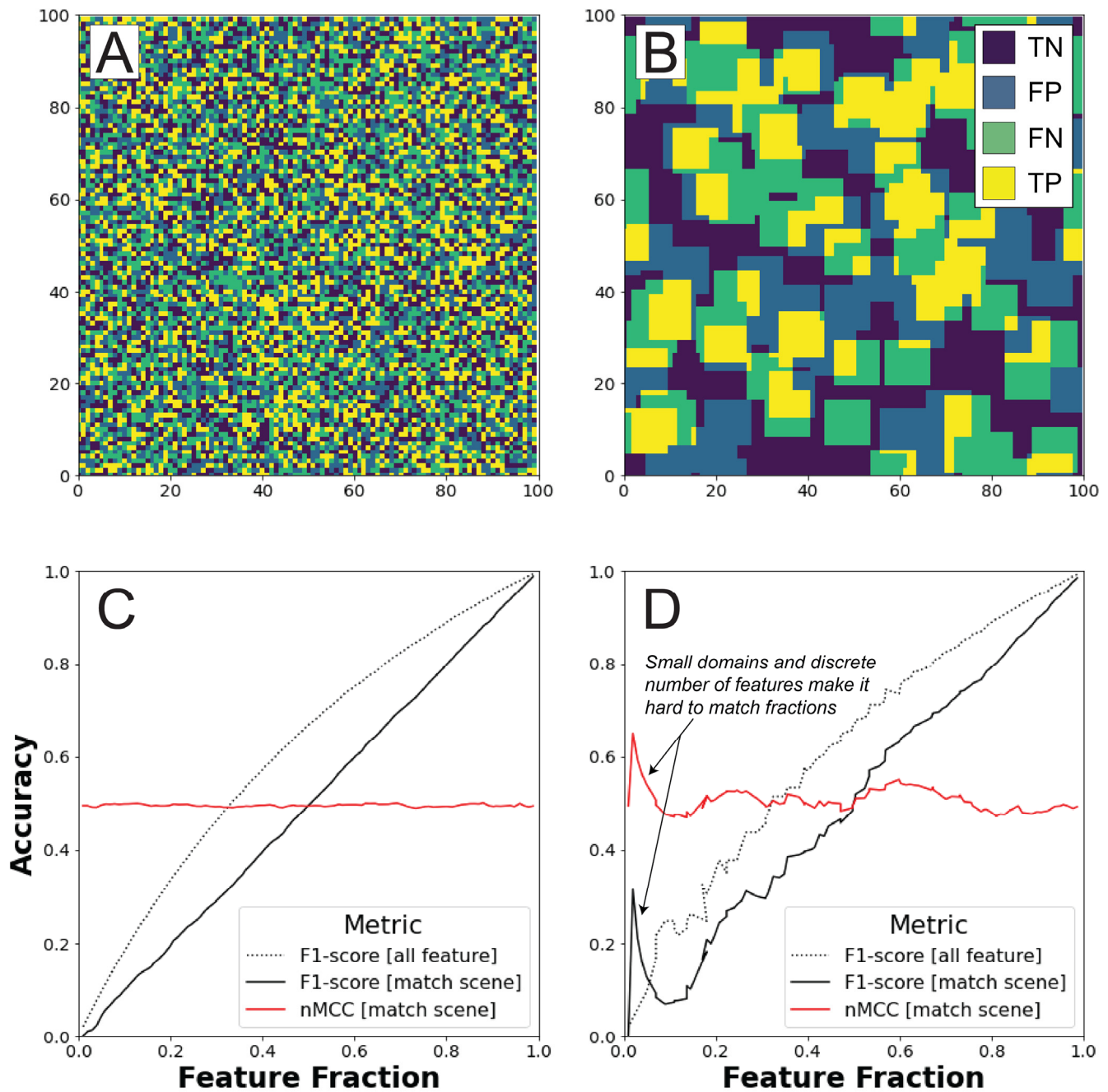


**Figure 3:** Classified 100 x 100 m maps of (A) 1-m and (B) 10-m long incipient features showing the four classification outcomes (*TN*: True Negatives, *FN*: False Negatives, *FP*: False Positives, *TP*: True Positives). How accuracy scores vary as a function of feature fraction are also shown for (C) 1-m and (D) 10-m long incipient features, respectively. The ‘all feature’ scenario is where the model assumes the entire surface is feature with no matrix, regardless of scene-level properties. The ‘match scene’ scenario is where the model data matches the actual feature fraction, but whose feature locations are independent of each other. In A-B, example maps are shown for the case where fifty percent of the

310

surface is covered by features. In C-D, *normalized Matthews Correlation Coefficient (nMCC)* is only shown for the 'match scene' scenario because it is undefined in the 'all feature' scenario.

315

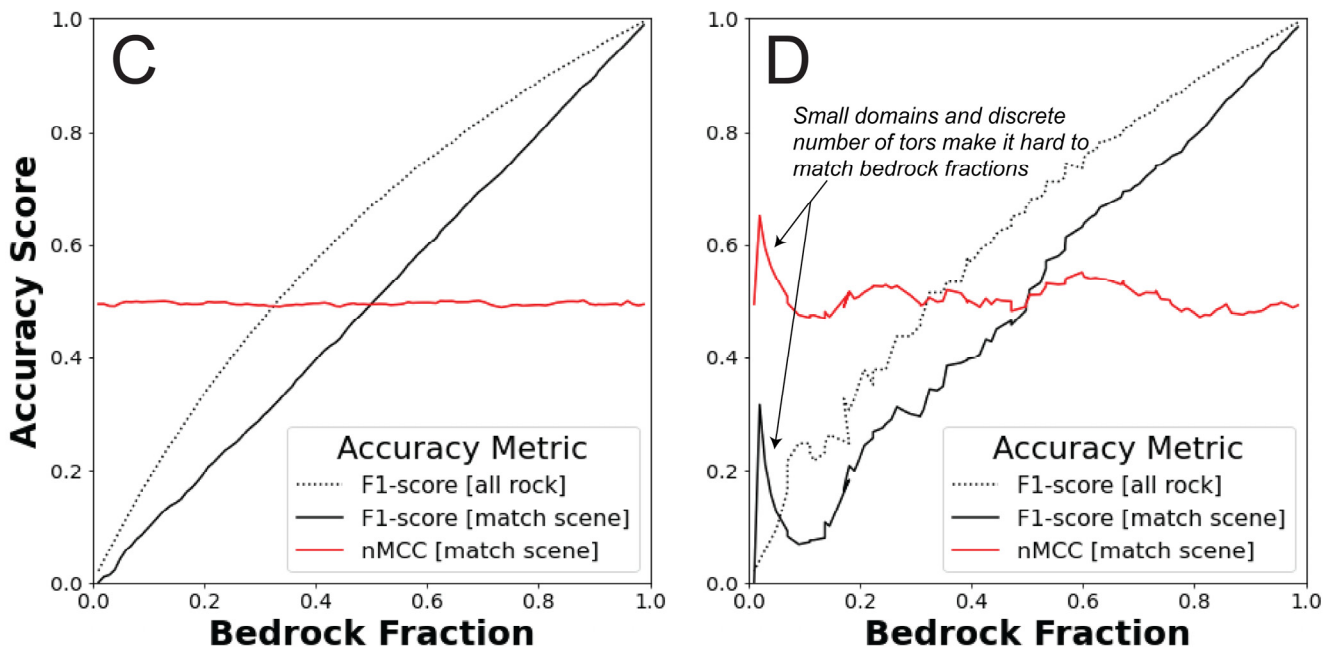
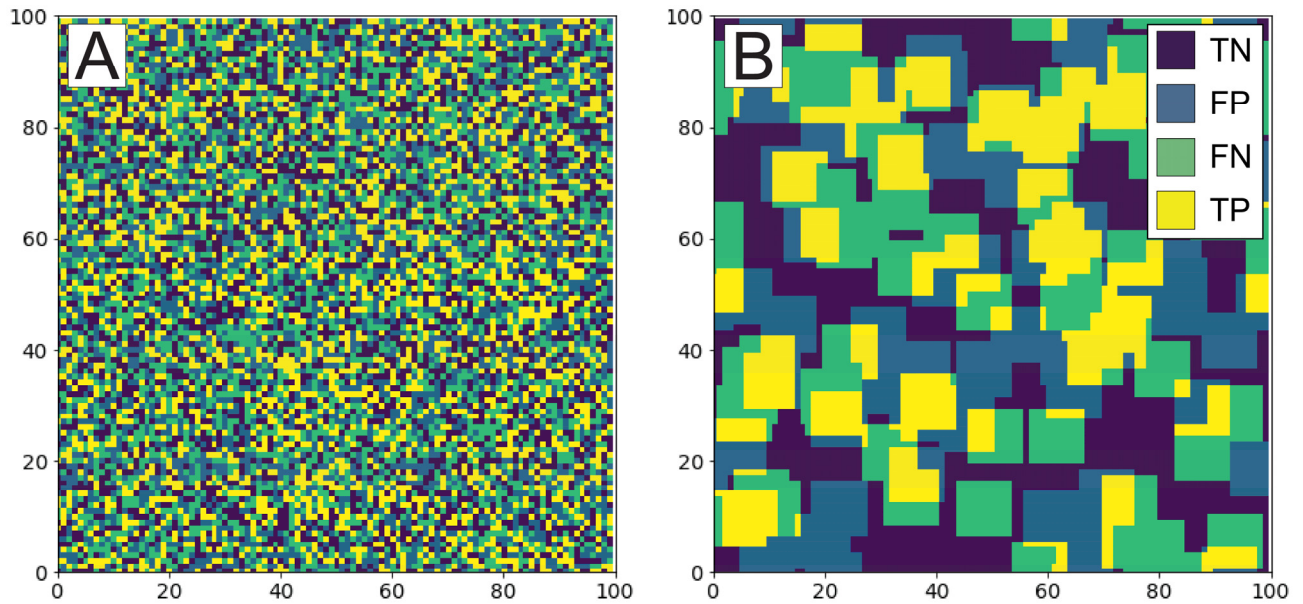
Figure 3 shows the sensitivity of *F1-score* and *nMCC* to ~~a research design that tests binary classifiers across gradients in bedrock fraction for a typical scene~~ imbalanced data when the model and truth data are independent from each other ( $m = n = 100$ ). ~~Two scenarios are considered.~~ Each ~~assume bedrock outcrop~~ scenario assumes features are randomly distributed throughout the scene for any given ~~bedrock~~ *feature* fraction. In the first scenario, the ~~bedrock~~ classifier predicts that ~~bedrock~~ *the feature* is found everywhere regardless of the truth data (dashed lines). Because this 'all ~~rock~~ *feature*' model produces neither False Negatives nor True Negatives, *nMCC* is undefined in this scenario (see eqs. 6-7). *F1-score* nonlinearly improves with increasing ~~bedrock~~ *feature* fraction and approaches unity as the actual ~~bedrock~~ fraction nears the 'all-~~rock~~ *feature*' model. In the second scenario, the ~~bedrock~~ classifier is forced to match the ~~bedrock~~ *feature* fraction in the truth grid, though the locations of ~~bedrock outcrop~~ *features* in the model are independent from the truth data (solid lines). This represents a worst-case scenario for a classifier that successfully models the scene-level fraction ~~of bedrock~~ while also providing zero predictive value at the pixel level. The values of *nMCC* rightly diagnose independence between the model and truth data by showing zero correlation across the full range of ~~bedrock~~ *feature* fractions ( $nMCC \sim 0.5$ ). In contrast, *F1-score* increases as a linear function of ~~bedrock~~ *feature* fraction. As this and subsequent examples show, *F1-score* embeds a spurious correlation with ~~bedrock~~ *feature* fraction, all other things being equal, because the number of True Negatives is ignored. In contrast, *nMCC* provides a robust metric to evaluate positional error for classifiers that have been calibrated to scene-level properties ~~like bedrock fraction~~. While these relationships do not depend on ~~to~~ *incipient feature* size, larger mapping areas are needed to adequately sample the statistics of feature locations when incipient ~~to~~ *features* are large with respect to the area of the scene (Fig. 3D). The noisy relationships in Figure 3D largely reflect the inability to match the specified ~~bedrock~~ *feature* fraction using a discrete number of random ~~to~~ *features* whose locations are set by the specific pseudo-random seed used. In fact, 49% of the grids generated for Figure 3D failed to meet the 0.5% tolerance of specified ~~bedrock~~ *feature* fractions after fifty iterations. For subsequent analyses, ~~I use larger scenes of~~ 1000 x 1000 m ~~scenes are used~~ to mitigate the effect of domain size on accuracy scores. For ~~this~~ *the* larger domain, nearly all (>99%) the subsequent grid pairs meet the tolerance criterion before fifty iterations, which manifest as smoother curves in plots.

320

325

330

335



340 **Figure 3:** Classified 100 x 100 m maps of (A) 1 m and (B) 10 m long square tors showing the four classification outcomes (*TN*: True  
 345 *Negatives*, *FN*: False Negatives, *FP*: False Positives, *TP*: True Positives). How accuracy scores vary as a function of bedrock fraction are  
 also shown for (C) 1 m and (D) 10 m long tors, respectively. The ‘all rock’ scenario is where the model data assumes the entire surface is  
 bedrock regardless of the actual bedrock fraction. The ‘match scene’ scenario is where the model data matches the actual bedrock fraction,  
 but whose locations are independent. In A–B, example maps are shown for the case of 0.5 bedrock. In C–D, normalized Matthews Correlation  
 Coefficient (*nMCC*) is only shown for the ‘match scene’ scenario because it is undefined in the ‘all rock’ scenario.

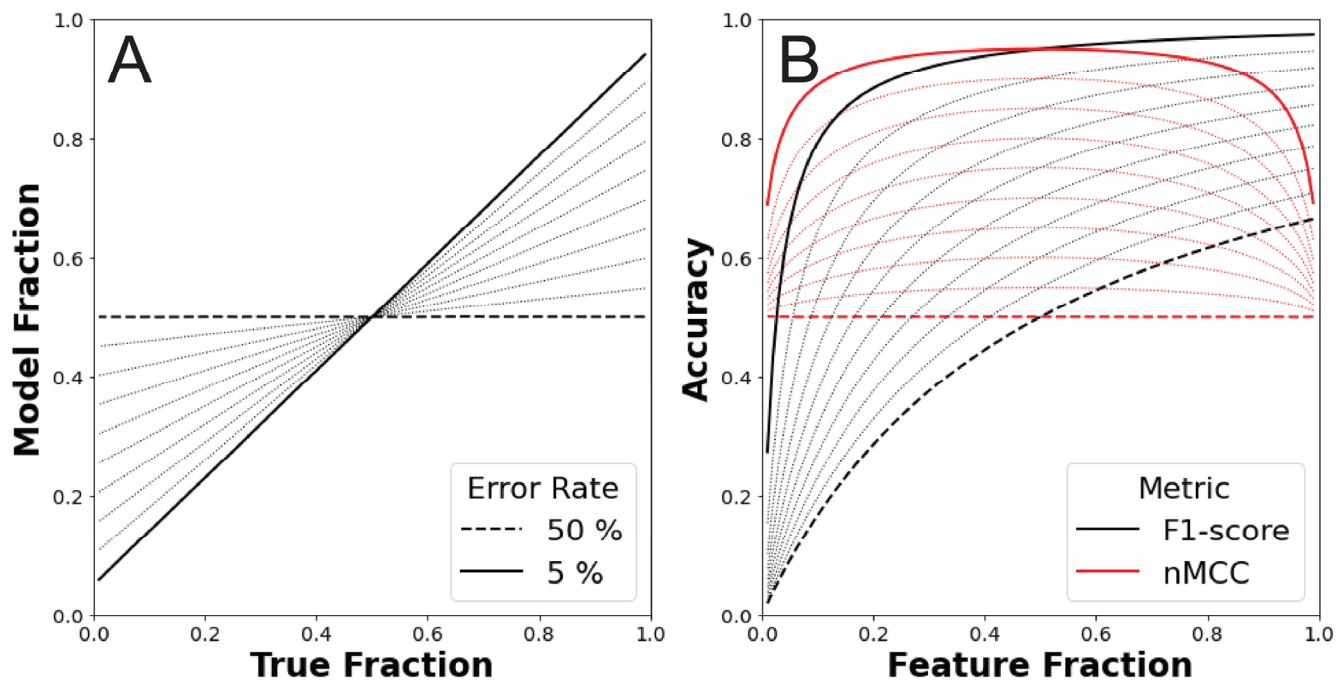


## 54 Error structure and accuracy

In the previous section, I showed how  $F1$ -score and  $nMCC$  vary as a function of bedrock fraction for very poor pixel level feature prevalence for classifiers. A that only honoured scene-level attributes (i.e., feature fraction) with no predictive skill at identifying feature locations. While a useful baseline scenario, a good classifier though, whether statistically or physically based, should be successful in most cases identify both the locations of features and reproduce scene-level attributes, albeit with some residual error. To illustrate these more realistic conditions, I consider three different error scenarios are presented where the error structure is either random (section 54.1), systematic (section 54.2), or both (section 54.3). While actual sources of error are in geomorphic studies are typically more complex (e.g., Fig. 1), these endmembers simple scenarios are intended to facilitate interpretation and provide a heuristic understanding for insight into how pixel-level accuracy scores perform when the research design explicitly samples across a gradient in feature prevalence.

### 54.1 Random error

The first error scenario I consider considered is the situation where the binary classifier successfully identifies bedrock feature locations with a fixed rate of random error ( $\bar{e}_r$ ). To create synthetic surfaces of this type, a truth grid is first generated (for Fig. 4  $m = n = 1,000$ ) for a given bedrock feature fraction. Bedrock to Features are assumed to occupy a single pixel, though results are robust to different sizes of incipient to features because the where error location occurs is independent of feature location locations. To produce the associated model grid, I an error grid is first generated an error grid using a different pseudo-random seed than that used to generate the bedrock grid truth data. The grid of continuous values is of the error grid are converted to binary classes (0 = no error; 1 = error) using the specified error rate as the threshold. The error grid is then used to construct the model grid from the truth grid by flipping bedrock feature classifications wherever the error grid value equals one. Note that the maximum error rate shown in Figure 4 is 0.5 fifty percent. This is the scenario where the truth and model data are least correlated. Increasing the error rate further will produce increasingly stronger negative correlations between the model and truth data. Once both truth and model grids are generated,  $F1$ -score and  $nMCC$  are calculated. This analysis is done for bedrock feature fractions that range from 0.01 to 0.99 and error rates from 0.055 to 0.550 percent.

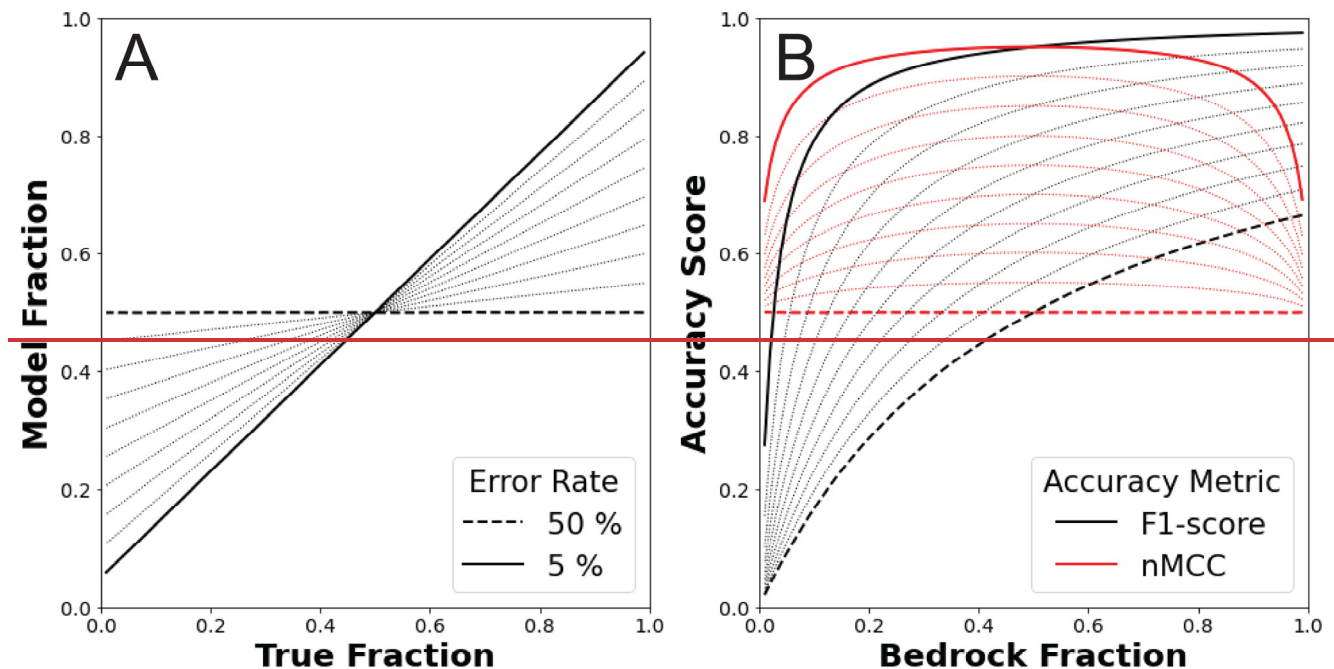


370 **Figure 4:** (A) Model feature fractions and (B) associated accuracy scores as a function of the true feature fraction in the random error scenario (1000 x 1000-m map area). In both plots, the minimum and maximum error rates are highlighted, and 5% increments of error rate are shown as dotted lines. In A, matching the model fraction to the actual fraction of bedrock is not enforced like in other scenarios (Figs. 3, 5). However, the two fractions are linearly related, and the slope of the relationship is directly related to the error rate. In B, lower rates of random error amplify the nonlinearity between *F1-score* and feature fraction while *nMCC* more uniformly improves across a broad range of feature fractions.

380 **Figure 4 shows** the results of this analysis for ten different numerically simulated error rates in Figure 4. These results. Results can be derived analytically from eqs. 5-7 and the imposed random error rate (Appendix A). However, presenting the results from synthetic landscapes numerical surfaces: 1. To ensure Ensures that synthetic scenes adequately sample population statistics; and 2. Facilitate Facilitates integration with scenarios that include non-random error (section 5.3). As should be expected, Figure 4 shows that accuracy scores increase with lower error rates go down. However, the sensitivity of these scores is not uniform with respect to bedrock feature fraction. Much like in the previous example scenario (Fig. 3), *F1-scores* always monotonically improve with increasing bedrock feature fraction. Note here though that the worst random error case (Fig. 4 dashed black line; 50% error rate) is not equivalent to the case where the model is independent from the truth data (i.e., the solid black line in Fig. 3). In the random error scenario, model data are correlated with, but not equal to, actual bedrock feature fractions (Fig. 4A). The fixed error rate preferentially modifies the larger frequency class when near the endmember cases of all bedrock zero and all soil full coverage of the surface by features. This behaviour is most easily envisioned for the case where at the error rate is 50% limits of feature abundance. If the actual surface is all bedrock features,

then the ~~model produces 50% soil on average, and visa versa~~ random model will produce matrix pixels in proportion to the error rate. Similarly, if the actual surface is all ~~soil. In matrix, then~~ the random error model will produce feature pixels in proportion to the error rate. For this error scenario, the slope of the relationship between modelled and actual ~~bedrock feature fractions~~ equals  $1 - 2\bar{e}_r$  (Appendix A). The symmetry of the sensitivity of  $nMCC$  to a ~~constant uniform, random~~ error rate allows for comparison of map accuracies across a wide range of ~~differentially balanced data feature abundances~~, specifically over the domain over which  $nMCC$  is approximately invariant (Fig. 4B). In contrast, disentangling the spurious correlation between  $F1$ -score and ~~bedrock feature~~ fraction interacts with the preferential modification of ~~surface~~-classes in a complex way, leading to increasing nonlinearity ~~in response to~~ for better classifiers with lower error rates.

395



400 **Figure 4:** (A) Model bedrock fractions and associated (B) accuracy scores as a function of true bedrock fraction for the random error scenario (1000 x 1000 m map area). In both plots, the minimum and maximum error rates are highlighted, and 5% increments of error rate are shown as dotted lines. In A, matching the model fraction to the actual fraction of bedrock is not enforced like in other scenarios (Figs. 2, 5). However, the two fractions are linearly related, and the slope of the relationship is directly related to the error rate. In B, lower error rates amplify the nonlinearity between  $F1$ -score and bedrock fraction while  $nMCC$  more uniformly improves across a broad range of bedrock fractions.

405

#### 54.2 Systematic error

The second error scenario ~~I consider~~ considered is the situation where the binary classifier successfully identifies ~~bedrock features~~ with ~~some imposed~~ systematic error. This scenario is motivated by the common challenge of aligning two ~~datasets collected using different sensors or collected at different times (e.g., Bertin et al., 2022)~~. To create synthetic surfaces of this type, a truth grid is first generated (for Fig. 5  $m = n = 1,000$ ) for a given ~~bedrock feature~~ fraction and ~~to incipient feature~~ size. Incipient ~~to s features~~ are randomly distributed throughout the model domain. To ~~generate~~ produce the associated model

410

grid, a copy of the truth grid is linearly offset by one pixel to the right in the x-direction, though results are insensitive to the direction of the shift. By using wrap-around boundaries, synthetic truth and model grids always have an identical bedrock fraction-feature fractions. Note that the systematic error rate ( $\bar{e}_s$ ) is not constant and is instead a function of the bedrock fraction, the magnitude of the systematic offset, and the shape and size of features. Once both truth and model grids are generated, *F1-score* and *nMCC* are calculated. This analysis is done for bedrock fractions that range from 0.01 to 0.99 and for incipient feature sizes that range from 1x1 m to 10x10 m squares (i.e., areas of 1 to 100 pixels).

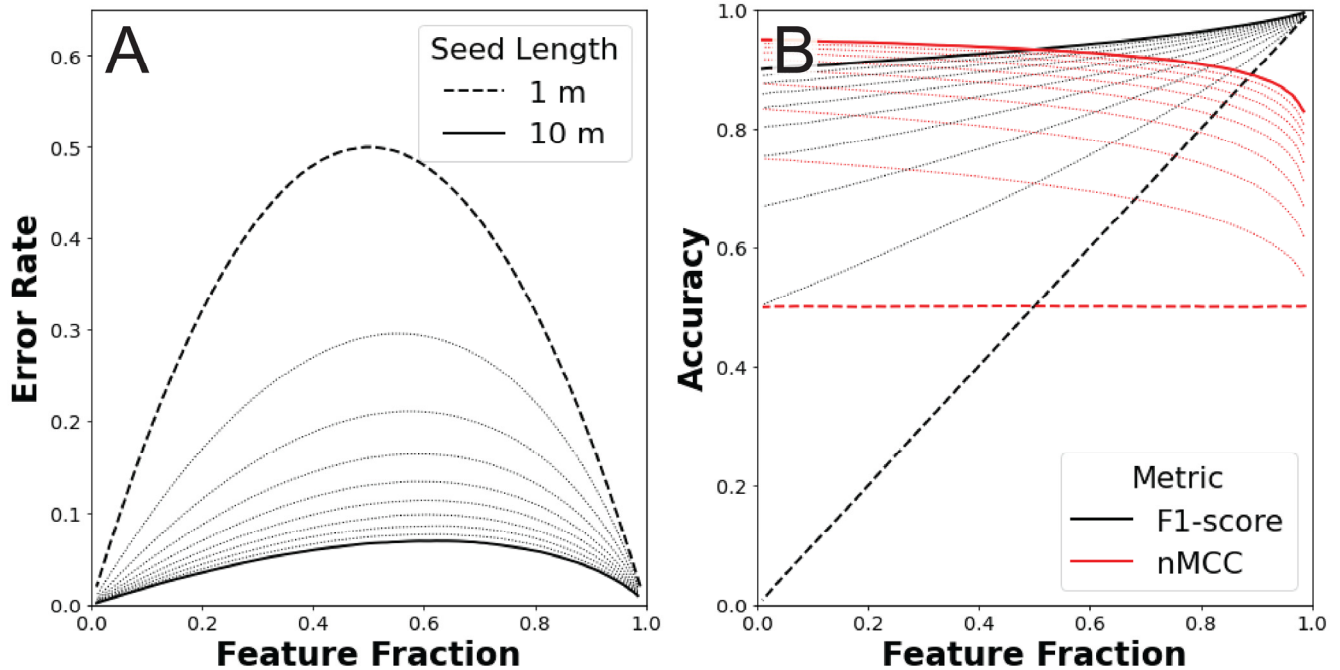
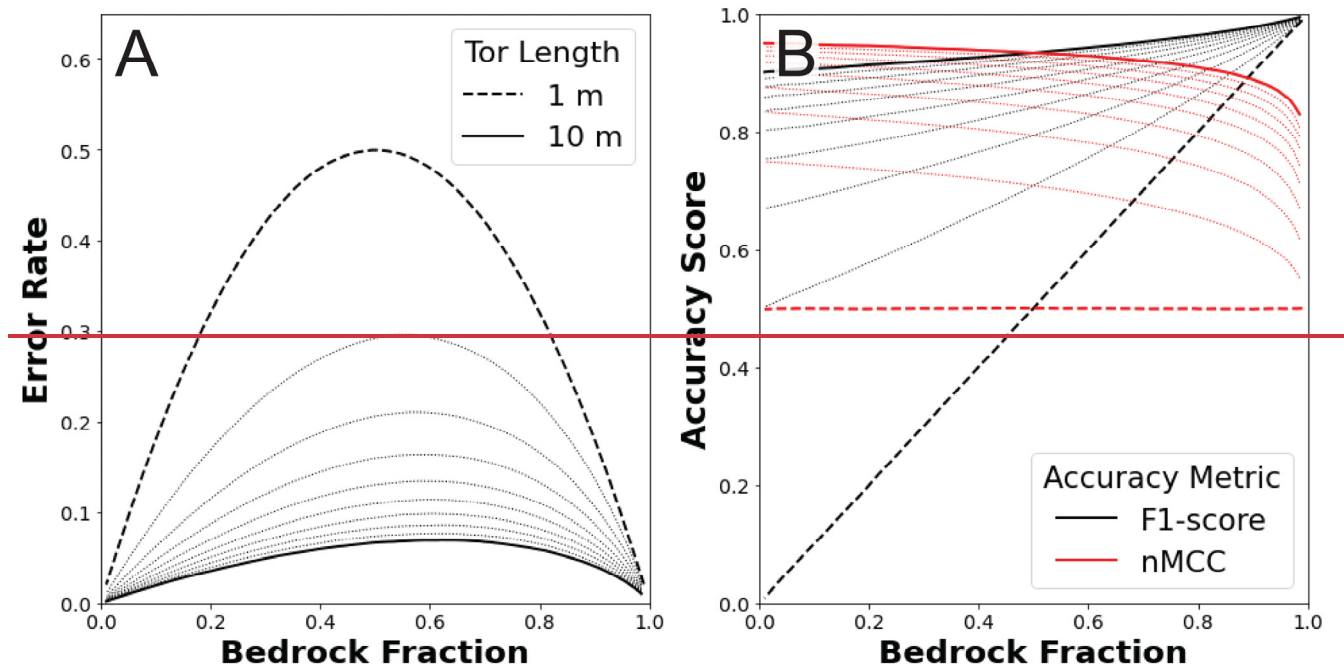


Figure 5: (A) Variable error rates and (B) associated accuracy scores as a function of the true feature fraction for the systematic error scenario (1000 x 1000 m map areas). In both plots, the minimum and maximum incipient feature lengths are highlighted, and 1-m increments are shown as dotted lines. In A, the error rate (eq. 2) is non-uniform with lower rates at both low and high feature fractions. As incipient feature size gets larger, the error rate function becomes increasingly asymmetrical with peak values at 0.5 and 0.66 bedrock for 1- and 10-m long seeds, respectively. In B, the non-uniform error rates lead to more linear relationships between *F1-score* and feature fraction than in the case of random error (Fig. 4B). In contrast, *nMCC* shows modest negative relationships with feature fraction for all incipient feature sizes.

Figure 5 shows the results of this analysis for ten different incipient seeds that span from 1 to 10 m in length (1 to 100 m<sup>2</sup>). While these results throughout this paper are discussed in terms of a scale typical to airborne lidar (i.e., 1-m spatial resolution), the relationships shown here are better cast as the ratio of the incipient feature scale (i.e., seed length in pixels) to the error scale (1 pixel length) where the feature detection limit is one pixel. When the systematic error is

of order feature length, systematic error mimics the case where the truth and model data are independent (e.g., compare long dashed lines in Fig. 5B to solid lines in Fig. 3C-D). As the systematic error gets smaller with respect to the incipient feature size, both *FI-score* and *nMCC* improve. The largest improvements occur for small incipient feature sizes and at low bedrock fraction (Fig. 5B). When bedrock fractions are low, the error is largely due to the geometric effect of the shift of individual square objects surrounded by soil such that  $TP = \frac{t^2 - t}{t^2}$  and  $FP = FN = \frac{t}{t^2}$  (Appendix B)-matrix. As bedrock fraction increases, incipient objects increasingly coalesce into a smaller number of feature objects, and the error is set by these more complex geometries (see discussion in section 6.2). Figure 5A shows how that increasing the incipient feature size leads to lower error rates and increasing asymmetry in the error as a function of bedrock fraction. Error, where the highest error is biased towards higher feature abundances. These error rate functions skew towards higher bedrock fractions leading to a modest negative relationship between *nMCC* and bedrock fraction regardless of incipient feature size (Fig. 5B). The asymmetric error structure also impacts *FI-score*, albeit in a way that is much harder to diagnose due to the spurious correlation between *FI-score* and bedrock fraction (Figs. 3-4). The notion of systematic error in scene-level mapping was envisioned for situations where co-registration error between the remote sensing data used to map ‘truth’ and the remote sensing data used to build the classifier produce a systematic, translational offset. Strictly speaking then, this synthetic scenario represents the case where a translational offset is the same for all scene-level patches, a plausible situation if the truth and model data for different scenes were acquired at the same time and in the same way. However, even under the less stringent condition where co-registration errors are oriented differently in different scenes (i.e., due to different acquisition parameters and times), the relationships shown in Figure 5 will still hold as long as the magnitude of the systematic error is similar across sites and there is no preferred orientation of features is isotropic to feature objects.



455 **Figure 5:** (A) Error rate response to tor size and associated (B) accuracy scores as a function of the true bedrock fraction for the systematic error scenario (1000 x 1000 m map areas). In both plots, the minimum and maximum tor lengths are highlighted, and 1 m increments are shown as dotted lines. In A, the error rate (eq. 2) is non-uniform with lower rates at both low and high bedrock fractions. As tors get larger, the error rate function becomes increasingly asymmetrical with peak values at 0.5 and 0.66 bedrock for 1- and 10-m long tors, respectively. In B, the non-uniform error rates lead to more linear relationships between *F1-score* and bedrock fraction than in the case of random error (Fig. 4B). In contrast, *nMCC* shows modest negative relationships with bedrock fraction for all incipient tor sizes.

460 **54.3 Random plus systematic error**

The third error scenario ~~I consider~~considered is the situation where the binary classifier is systematically offset from the truth grid with an additional random error term. To create synthetic surfaces of this type, a truth grid is first generated (for Fig. 6 m = n = 1,000) for a given bedrock feature fraction ( $f_b$ ) and tor incipient feature size. Tors~~Incipient features~~ are randomly distributed throughout the model domain. To generate~~produce~~ the associated model grid, a copy of the truth grid is first linearly offset by one pixel to the right in the x-direction, using a wrap-around boundary condition. ~~I then generate a~~A random error grid is then generated using a different pseudo-random seed than that used to generate the bedrock grid~~truth data~~. The grid of continuous values is of the error grid are converted to binary classes (0 = no error; 1 = error) using a random error rate of 0.05 as a threshold. The random-error grid is ~~then~~-used to flip bedrock-classifications in the offset feature grid wherever the error grid value equals one. Note that model bedrock feature fractions in the model need not match the truth data, and error rates will are now be a function of the bedrock feature fraction, the magnitude of the systematic offset, the size and shape and size of bedrock features, and the random error rate. Once both truth and model grids are generated, *F1-score* and *nMCC* are calculated. This analysis is done for bedrock feature fractions that range from 0.01 to 0.99 and tor incipient feature sizes that range from 1x1 m to 10x10 m squares (e.g., areas of 1 to 100 pixels).

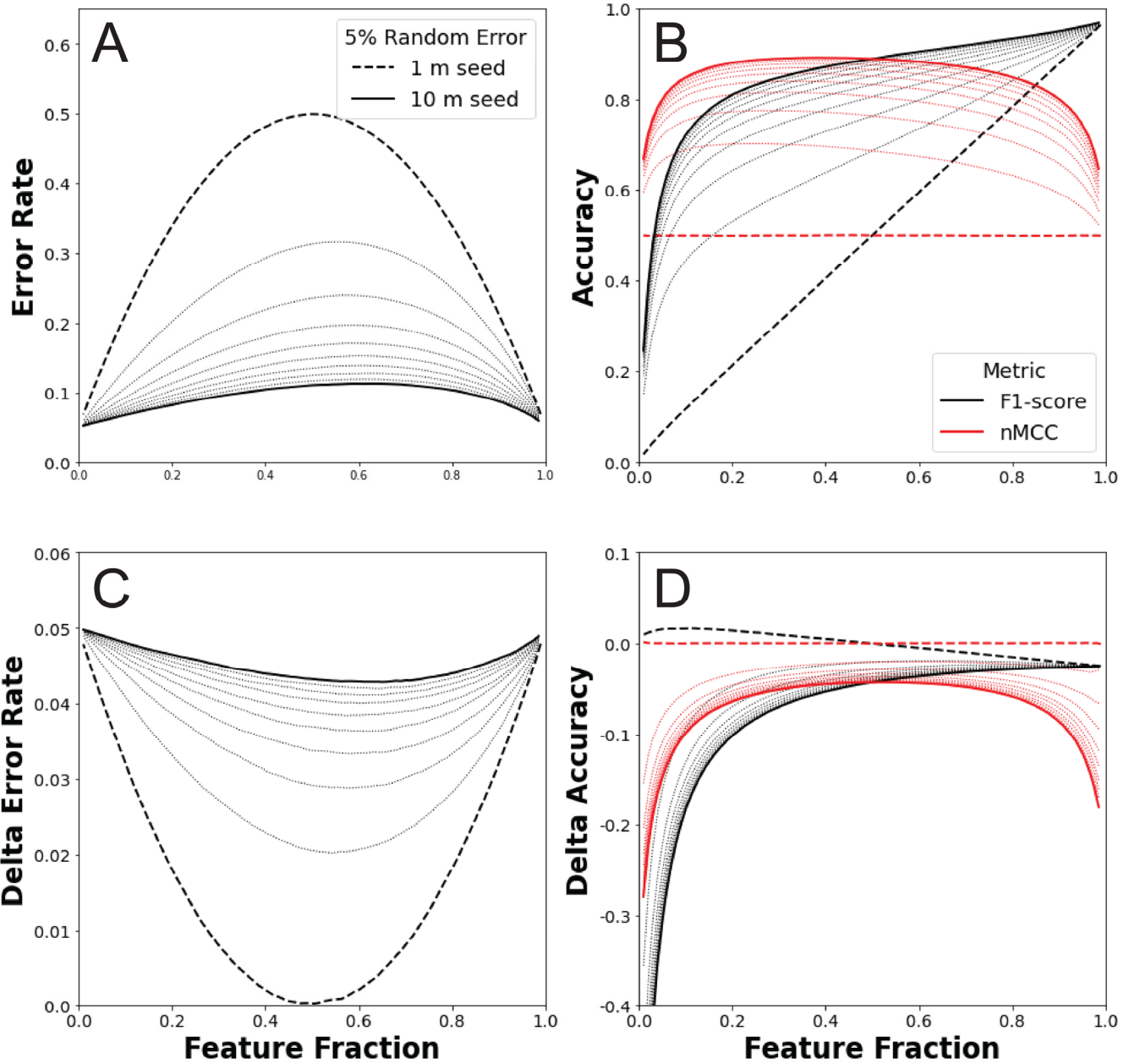


**Figure 6:** (A) Variable error rates and (B) associated accuracy scores as a function of the true feature fraction for the systematic plus random error scenario (1000 x 1000-m map areas). These panels are analogous to Figure 5A and 5B but now include a 5% random error term. Differences in (C) error rates and (D) accuracy scores between this scenario and systematic error alone (Fig. 5) are shown to enable comparison. In C, the additional 5% random error term is linearly added to the systematic error term at the endmember cases of zero and total feature coverage. The random error translates into something less than 5% for intermediate cases with minima near zero for 1-m seeds

and 0.043 for 10-m seeds. In D,  $nMCC$  exhibits strong reductions from systematic error alone near endmember cases (high negative values) and a muted, more uniform reduction at intermediate values.

485

Figure 6 is analogous to Figure 5 with error rates (Fig. 6A) and accuracy scores (Fig. 6B) plotted as a function of bedrock feature fraction for different incipient features sizes. The random error rate sets the minimum observed error and contributes to the total error in a nonlinear nonuniform way. This is because the random error term can flip values where systematic error occurs has occurred (i.e., both sources of error can combine to produce True Positives). Figure 6C ~~and 6D show~~ D shows the differences in error rates and accuracy scores, respectively, between systematic error alone (Fig. 5A-B) and the systematic error plus random error scenario shown here (Fig. 6A-B) and systematic error alone (Fig. 5A-B). The addition of random error is relatively more influential in cases where the classifier is more accurate (i.e., larger incipient features) and near endmember bedrock fractions (i.e., all soil zero and all rock total coverage of features). For a given incipient feature size, the minimum error added by the random error rate of 0.05 occurs at intermediate bedrock fractions and ranges from near zero for 1-m long seeds to 0.043 for 10-m seeds. The results shown in long seeds. Figure 6B ~~show~~ 6 shows that relationships between pixel-level accuracy scores and scene-level bedrock fraction for this scenario include elements the relative importance of both the random error and versus systematic error scenarios changes as a function of feature fraction. Because random error is the dominant term of the total error rate near the endmember cases of zero and all bedrock total feature coverage, it leads to correspondingly large reductions in  $nMCC$  (Fig. 6D). In contrast, at intermediate bedrock fractions there is slight negative slope to  $nMCC$  like observed in the systematic error scenario (Fig. 5B). This is because reductions in  $nMCC$  induced by random error at intermediate bedrock feature fractions are: relatively smaller, approximately invariant across a broad range of fractions, and symmetrical with respect to bedrock feature fraction (Fig. 6D). While ~~I only show~~ one random error rate is shown, this example shows illustrates how the complex interactions between random and systematic error can need to be readily simulated to understand their implications on pixel-level accuracy scores.

## 505 5 Discussion

Whether mapping orographic gradients in bedrock exposure (Rossi et al., 2020), characterizing precipitation controls on termite mound density (Davies et al., 2014), or inferring how wind extremes induce tree throw frequencies (Doane et al., 2023), lidar topography has revolutionized our ability to map differences in the density of fine-scale features. None of these examples used pixel-level accuracy scores in their analyses. In fact, it is not immediately apparent how well such methods would perform even if the authors had adopted pixel-level accuracy assessment. For those geomorphic studies that have used pixel-level accuracy scores on lidar-based classifiers (e.g., Bunn et al., 2019; Clubb et al, 2014; Milodowski et al., 2015), it is not obvious how accuracy scores are expected to vary as a function of feature prevalence. To help address this challenge, this paper presented a suite of synthetic scenarios that show how  $F1$ -score and Matthews Correlation Coefficient ( $MCC$ ) perform across

510



515 gradients in feature prevalence when the error structure between model and truth data are known. While the scenarios are simple, they provide insight into how well suited, and under what conditions, two of the most widely used accuracy metrics are when data is imbalanced (5.1). The systematic error scenarios further revealed a strong sensitivity of accuracy metrics to the shape and size of feature objects (5.2). Finally, the results from synthetic scenarios are used to provide a tentative set of best practices for using pixel-level metrics in geomorphic studies (5.3).

### **5.1 Accuracy assessment for imbalanced mapping tasks**

520 One main goal of this study was to understand the sensitivity of *F1-score* and *MCC* to feature prevalence. It is useful for accuracy scores to be invariant with respect to feature fraction under a given error structure so that classified scenes can be calibrated and validated using a wide range of geomorphic settings. For example, Matthews Correlation Coefficient (*MCC*), and its normalized equivalent (*nMCC*), readily diagnosed the case of independence between truth and model data across the full range of feature abundances (red lines in Fig. 3). In contrast, a spurious correlation between feature abundance and *F1-score* was only exacerbated by adding scene-level constraints to this case (black lines in Fig. 3). Because *F1-score* only considers True Positives, False Positive, and False Negatives, it is an asymmetric accuracy metric (Table 1). Asymmetry refers to the fact that the score is dependent on the choice of target class. All pixel-level assessments that do not consider all four components of the confusion matrix (e.g., precision, recall, F-measures, receiver operating characteristic curves) are asymmetric. Asymmetric metrics may not be problematic if one outcome is much more important than its alternative due to its consequences (e.g., a medical diagnosis). However, for many of the geomorphic mapping applications posed here, the relative importance of one class over the other is unclear (e.g., bedrock versus soil; mound versus inter-mound; incised versus un-incised). Successfully identifying both the occurrence and non-occurrence of features is important. In multi-class accuracy assessment, it is common to calculate a ‘macro’ *F1-score*, which is the arithmetic mean of *F1-scores* for all classes. This macro averaging can also be applied to binary tasks by calculating the *F1-score* for the alternative case when target classes are swapped (Sokolova and Lapalme, 2009). While a macro *F1-score* for binary classification is symmetrical and easy to calculate, adoption of this approach is still relatively rare (Chicco and Jurman, 2020).

525

530

535

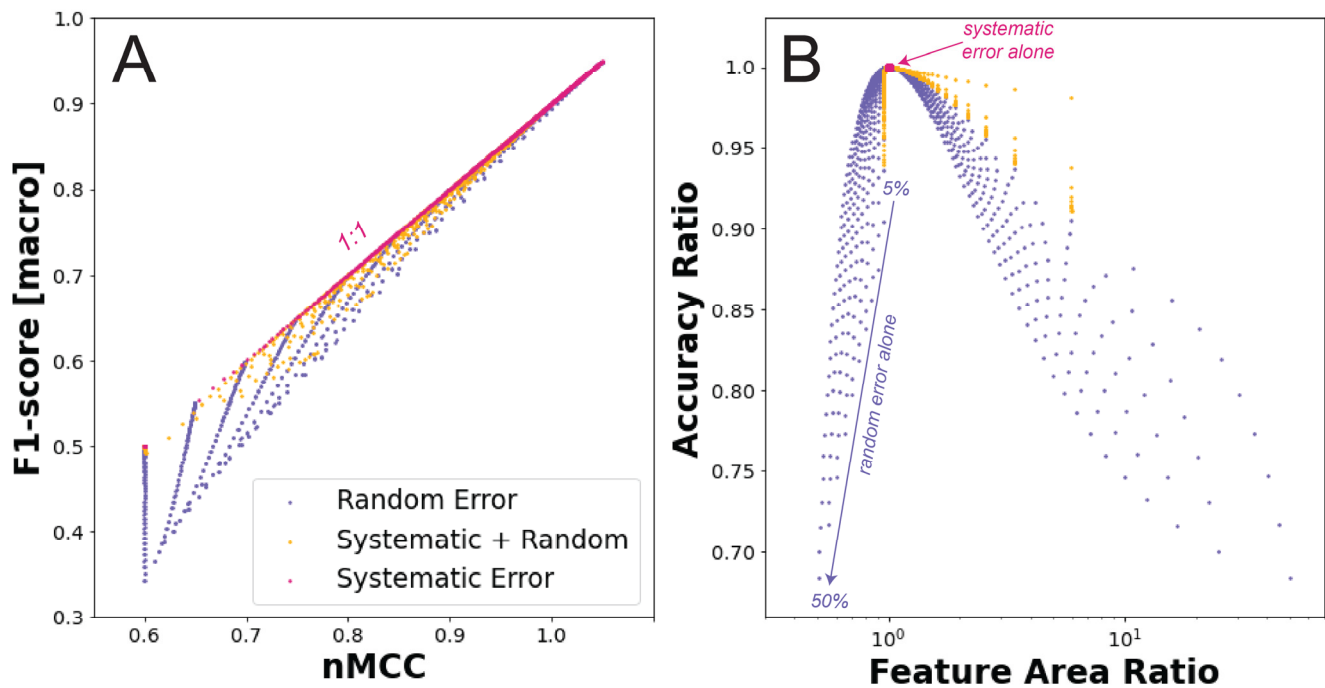


**Figure 7:** (A) Relationship between  $nMCC$  and macro  $F1$ -score for all the error scenarios posed in this study. (B) Ratio of accuracy scores ( $nMCC / \text{macro } F1\text{-score}$ ) as a function of feature area ratios (model area / true area). In A, the macro score is the arithmetic mean of the two  $F1$ -scores calculated when classes are swapped. In B, the ratio of scores is plotted as a function of the ratio of feature areas to show that when the model and truth data exhibit different scene-level properties (e.g., feature areas or fraction), the macro  $F1$ -score produces lower values. The systematic error scenario enforced the property that model and truth data match scene-level fractions which is why they all plot at the coordinates [1,1]. The other error scenarios often produced mismatches between scene-level feature fractions. In these cases, the accuracy metrics are only equivalent when the scene-level fractions match.

540

545

Figure 7 shows how macro  $F1$ -scores compare to  $nMCC$  for each of the error scenarios considered in this paper. This modified version of  $F1$ -score addresses the problem of asymmetry and produces similar values to  $nMCC$  when the error is small. In the systematic error scenario, the scene-level fraction of bedrock in the model data is identical to the truth data. This leads to a direct correspondence between  $nMCC$  and macro  $F1$ -score (red symbols in Fig. 7). However, for the scenarios that include a fixed rate of random error, the macro  $F1$ -scores generally plot below the 1:1 relationship (Fig. 7A). In these scenarios, accuracy metrics are only equivalent in cases where the scene-level fractions are the same between the model and truth data (Fig. 7B).

550

Notably, the systematic plus random error scenario produces accuracy metric ratios (Fig. 7B) closer to unity than random error alone for feature area ratios greater than one (low feature fractions). When feature area ratios are less than one (high feature fractions), accuracy ratios instead follow the trend defined by random error alone. Two important insights can be gleaned from Figure 7: (1) Even though macro  $F1$ -score addresses the problem of asymmetry, it penalizes random error more than  $nMCC$ , and (2) The mismatch between macro  $F1$ -score and  $nMCC$  is encoding disparities between scene-level and pixel-level measures of accuracy, albeit in a highly nonlinear way. Given that macro  $F1$ -score produces stronger sensitivity than  $nMCC$  to the random error scenarios (i.e., accuracy ratios < 1),  $nMCC$  should still be favoured as a more stable metric when

555

560 calibrating and validating feature classifiers across gradients in feature prevalence. However, and despite its relative success, caution is still warranted in comparing  $nMCC$  across gradients in feature fraction. Uniform, random error preferentially modifies the dominant class, leading to strong reductions in accuracy near endmember cases (Fig. 4; Appendix A). Even for relatively accurate classifiers, random error limits the domain over which  $nMCC$  is comparable (e.g., accuracy scores for 5% random error stabilize between ~20 to 80% feature abundances; Fig. 4).

565 The synthetic scenarios posed in this study were motivated by tasks where differences in scene-level feature abundances are driven by differences in geomorphic setting (e.g., due to climate, ecology, material property, erosion rate). As such, the synthetic surfaces generated for this analysis assumed that feature properties were homogeneously distributed *within* each scene (like the mima mounds in Fig. 1A). The key difference *across* scenes was feature prevalence, which was used to identify how sensitive accuracy metrics are to imbalanced data. However, the sensitivity of accuracy metrics to feature fraction also provides insight into how metrics might behave when features are heterogeneously distributed within a scene (like the bedrock and gully erosion maps in Fig. 1B-C). While it is beyond the scope of this analysis to systematically explore this, a simple thought experiment using the scenes generated from this study show why within-scene heterogeneity might be important to pixel-level accuracy assessment. There are many combinations of scenes with different feature fractions that can merge into a larger one with the same feature fraction. Table 2 shows a suite of examples that each produce 50 percent feature coverage.

575 **Table 2:** Merged scenes that produce fifty percent feature area\* [scene 1 percent / scene 2 percent].

	<u>5 / 95</u>	<u>10 / 90</u>	<u>15 / 85</u>	<u>20 / 80</u>	<u>25 / 75</u>	<u>30 / 70</u>	<u>35 / 65</u>	<u>40 / 60</u>	<u>45 / 55</u>	<u>50 / 50</u>
<u>Random</u>	<u>0.95</u>	<u>0.95</u>	<u>0.95</u>	<u>0.95</u>	<u>0.95</u>	<u>0.95</u>	<u>0.95</u>	<u>0.95</u>	<u>0.95</u>	<u>0.95</u>
<u>(5%)</u>	0.83 / 0.83	0.89 / 0.89	0.91 / 0.91	0.93 / 0.93	0.94 / 0.94	0.94 / 0.94	0.95 / 0.95	0.95 / 0.95	0.95 / 0.95	0.95 / 0.95
<u>Systematic</u>	<u>0.98</u>	<u>0.97</u>	<u>0.96</u>	<u>0.95</u>	<u>0.95</u>	<u>0.94</u>	<u>0.94</u>	<u>0.93</u>	<u>0.93</u>	<u>0.93</u>
<u>(10 m)</u>	0.95 / 0.86	0.95 / 0.89	0.95 / 0.90	0.94 / 0.91	0.94 / 0.91	0.94 / 0.92	0.94 / 0.92	0.94 / 0.93	0.94 / 0.93	0.93 / 0.93
<u>Sys + Rand</u>	<u>0.93</u>	<u>0.92</u>	<u>0.91</u>	<u>0.91</u>	<u>0.90</u>	<u>0.90</u>	<u>0.89</u>	<u>0.89</u>	<u>0.89</u>	<u>0.89</u>
<u>(10 m, 5%)</u>	0.80 / 0.75	0.85 / 0.80	0.87 / 0.83	0.88 / 0.85	0.89 / 0.86	0.89 / 0.87	0.89 / 0.88	0.89 / 0.88	0.89 / 0.89	0.89 / 0.89

\* The top row is the  $nMCC$  of merged scenes. The bottom row is the  $nMCC$  of each individual scene that was merged.

580 The merging of scenes in Table 2 helps illustrate how heterogeneous feature distributions may impact  $nMCC$ . For the random error scenario, the strong sensitivity to endmember cases is erased, and  $nMCC$  is uniform across all ten scene mixtures. For the systematic error scenario, accuracy improves for the higher feature fraction portion of the scene while accuracy marginally decreases for the lower feature fraction portions of the scene. For the systematic plus random error scenario, accuracy improves for both the higher and lower feature fraction portions of the scene. In all cases,  $nMCC$  is higher for the merged scenes than

585 for their constituent components, until they converge on each other when fully homogenous. While systematic error clearly induces non-uniform mixing (i.e., merged  $nMCC$  varies with different constituent feature fractions), all three cases suggest that heterogeneity generally favours more stable estimates of accuracy by sampling portions of the scene with both more and less abundant features. More thorough examination of this claim is needed. Taken at face value though, these results argue that it is better to train a model on all the data at once than on individual scenes with different feature fractions, if the source of classification error is expected to be similar. However, scene-level comparisons may provide more insight into variations in the error structure of the classification model itself, which is often poorly constrained.

590 Taken as whole,  $nMCC$  should be strongly preferred over  $FI$ -score when building and testing classifiers across gradients in feature abundance, with heterogeneous scenes and pooling of data perhaps favouring more stable assessment. Despite this result, the two scenarios that include systematic error also suggest that asymmetry in accuracy scores can still arise arising in response to the geometries and genesis of ~~more~~ features. In these cases, asymmetry is not due to limitations of the accuracy metric itself, but instead a result of how features are simulated in synthetic examples. Whether ~~my~~ the synthetic generative process (i.e., randomly distributed square ~~top~~ features of constant size) is representative of real transitions from ~~soil-~~ mantled ~~low~~ to ~~bedrock dominated hillsides~~ high feature fractions is an open question. ~~However that likely depends on the feature of interest. Nevertheless,~~ these synthetic examples provide an opportunity to probe how the evolution of feature geometries influence accuracy scores, a topic that is explored in much more depth below ~~and in Appendix B.~~

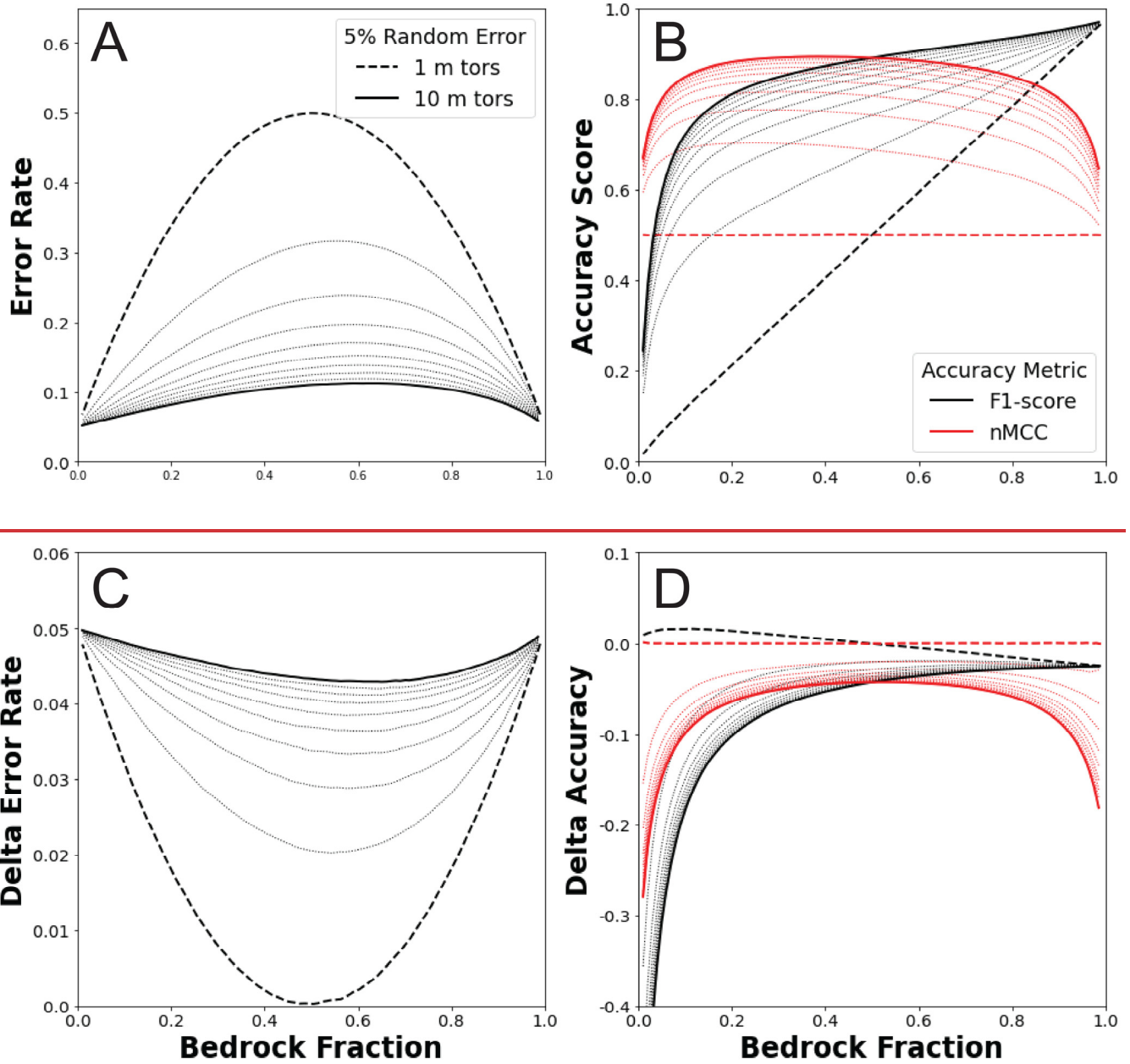


**Figure 6:** (A) Error rate response to tor size and associated (B) accuracy scores as a function of the bedrock fraction for the systematic plus random error scenario (1000 x 1000-m map areas). 5.2 Size and shape of features

The These panels are analogous to Figure 5A and 5B but now include a 5% random error term. Differences in (C) error rate and (D) accuracy scores between this figure and Figure 5 are shown to enable comparison. In C, the additional 5% random error term is linearly added to the systematic error term at the end-member cases of zero and all bedrock. The random error translates into something less than the 5% additional

error at intermediate cases with minima near zero for 1 m tors and 0.043 for 10 m tors. In D, *nMCC* exhibits strong reductions from systematic error alone near endmember cases (high negative values) and a muted, more uniform reduction for intermediate values.

## 6 Discussion

### 6.1 Accuracy assessment for imbalanced mapping tasks

Mapping patchy bedrock exposure is a good use case for binary classification on imbalanced data. Many studies have now had success doing scene level mapping of bedrock exposure using lidar topography (DiBiase et al., 2012; Heimsath et al., 2012; Marshall et al., 2014; Milodowski et al., 2015; Rossi et al., 2020). By calibrating lidar classifiers at the hillslope scale, there are enough observations to characterize the statistics and properties of bedrock features while also minimizing intra scene variations in climate, ecosystem, rock properties, and base level controls on soil production and denudation rates. Of this prior work, the only one to use pixel level accuracy scores to calibrate and validate their bedrock classifier was Milodowski et al. (2015). In their analysis, lidar classifiers were assessed at multiple roughness thresholds applied over different spatial neighbourhoods. Recognizing the challenges of imbalanced data, these authors subsampled the more frequent class in each scene to match the number of observations of the smaller class. My analysis shows that *Matthews Correlation Coefficient* (*MCC*) provides an alternative approach to handling the challenge of comparing scenes with different bedrock fractions that also addresses the problem of asymmetry embedded in other pixel level metrics (Table 1). While the limitations of metrics like *F1 score* are already well known (Chicco and Jurman, 2020), Figure 3 emphasizes an important implication of using this metric when the research design intentionally samples across scenes with differentially balanced data. Adding scene level constraints to a random classifier leads to lower *F1 scores* than simply assuming the entire surface is bedrock. In other words, adding scene level information in the calibration process actually reduces *F1 score*. This vulnerability is true for all pixel level assessments that do not consider all four components of the confusion matrix (e.g., *precision*, *recall*, *F measures*, *receiver operating characteristic curves*).

The results presented here corroborate arguments that *MCC* is generally a more robust pixel level accuracy metric than *F1 score* (Chicco & Jurman, 2020), specifically within the context of calibrating and validating bedrock mapping algorithms. Despite the improvements afforded by *MCC*, caution is still warranted in directly interpreting how pixel level metrics will vary as a function of feature prevalence. Uniform, random error preferentially modifies the dominant class, leading to strong reductions in accuracy near endmember cases, all other things being equal (Fig. 4; Appendix B1). Even for accurate classifiers, random error limits the domain over which *MCC*, and thus *nMCC*, can be confidently compared at the scene level (e.g., accuracy scores for 5% random error stabilize between ~20 to 80% bedrock; Fig. 4). Furthermore, linear regressions of observed and classified bedrock fractions (e.g., DiBiase et al., 2012; Rossi et al., 2020) can provide clues as to how error varies across scenes. Under the narrow conditions of uniform and spatially random error, the y intercepts of regressions should equal

640 the error rate and the regression slope should be less than one (Appendix A). The linear regressions presented in Rossi et al. (2020) were forced through the origin. Had they not been, the y-intercepts of those fits would have been negative, suggesting that the classified lidar data tended to produce more error at lower bedrock fractions. While the number of scenes analysed was small (8 scenes), this tendency towards higher error at lower bedrock fractions makes sense with respect to how bedrock emerges in the Colorado Front Range. Lower relief hillsides with less bedrock are dominated by tors as opposed to bands of bedrock cliffs that begin to emerge on higher relief hillsides. The myriad sources of error in real landscapes (Fig. 1) will lead to much more complex intra-scene error than either the random or systematic error scenarios posed here. Nevertheless, these simple scenarios provide a useful baseline for interrogating how spatially correlated error can be diagnosed from inter-scene differences in  $nMCC$ . With respect to systematic error, I only considered the case where truth and model data are offset by one pixel. Despite its simplicity, this exercise revealed that the scale of individual features matters when error is correlated to feature location. Systematic error scenarios produced an asymmetrical sensitivity of  $nMCC$  to the fraction of bedrock, a result that was not an artifact of ignoring components of the confusion matrix. This result begs the question as to what other properties of features are changing as a function of bedrock fraction that can explain the observed asymmetry (Figs. 5-6), a question which I explore in more depth below.

## 6.2 Size and shape of features

655 Up to now, the focus of this paper has largely been on what to expect from pixel-level accuracy scores when a binary classifier for bedrock is applied across a gradient in bedrock fraction. Embedded in this analysis are assumptions for how features emerge at higher bedrock fractions. Specifically, I assumed that the spatial distribution of incipient features is random. This treatment allowed me to probe how scene level and pixel level accuracy relate when sampling across large gradients in bedrock exposure. Features emerge at higher abundances. Intriguingly, a negative correlation between  $nMCC$  and bedrock fraction emerged in scenarios with systematic error, regardless of the incipient feature size (Fig. 5B; 6B). Given that  $nMCC$  addresses the problem of asymmetry with respect to target class (Fig. 3; Fig. 4B), what causes this asymmetrical sensitivity of  $nMCC$  to systematic error?

665 In all the scenarios I have presented, the minimum tor size is set by the tor length. Because incipient tors are placed on the surface by randomly placing their centres in the scene, more complex features are generated where incipient tors overlap by chance. To illustrate the implications of this approach, Figure 7 examines how feature size. One likely candidate is that the simulated changes in feature prevalence entailed a corresponding change in the size and shape: 1. Impact the error caused by a 1-pixel shift, and 2. Change as a function of bedrock fraction for the scenarios considered in this study. In general, error is expected to go down with increasing feature size because area increases faster than the length of the edge of the feature being offset. Due to the symmetry of the error induced by objects, a feature being offset by one pixel, recall, precision, and  $F1$  score are equivalent for this kind of systematic error (Fig. object is defined here as a spatially isolated occurrence of the target class (i.e., the ones in a binary classification) enveloped by pixels of non-occurrence (i.e., the zeros in a binary

classification). As features become more abundant, small objects coalesce into larger ones. This section probes the role of object size and shape on error by examining how the incipient feature shape interacts with translational error. I focus on these values as a measure of error induced by feature shape alone that is independent of the scene level bedrock fraction. As bedrock fractions increase in my synthetic surfaces, the average size of individual features gets larger. Whether this increase in feature size is due to changing the incipient tor size or the coalescing of many incipient tors into a single feature, *FI scores* always monotonically improve (Fig. 7B). However, Figure 7A nicely contrasts the differences in the error induced by a 1-pixel shift of simple features like square tors versus the more complex ones generated by the coalescing of incipient tors. For the same feature area, simple feature boundaries produce less error than sinuous, convex-concave boundaries because the area to edge ratio is higher, thereby minimizing the impact of translational offsets (see more examples in Fig. B1). Most shapes produce less error as they get larger, though it is possible to create shapes that produce more error as they get larger (see 'star' shape in Fig. B1). In the synthetic scenarios where there is systematic error, both the average feature area and *FI scores* increase with increasing bedrock fraction. The error looks like that of isolated square tors only at the lowest bedrock fractions. As features get larger, *FI score* substantially improves but at a lower rate than if bedrock was modelled as a single square tor (black line in Fig. 7B), reflecting the lower area to edge ratios produced by these complex feature shapes. Interpreting *FI score* is limited by the fact that it does not account for True Negatives, which necessarily go down as bedrock fraction goes up. As such, increasing bedrock fraction in my synthetic scenarios should record the trade-offs between increasing feature sizes leading to less error and increasing feature complexity leading to more error. The negative trends in *nMCC* shown in Figures 5B and 6B suggest that the net result of these competing effects is that increased complexity is the dominant term. The asymmetrical sensitivity of *nMCC* to systematic error also highlights the importance of how feature abundances are being simulated. Are the subsequent bedrock maps produced in this study representative of the actual transition from soil-mantled to bedrock-dominated hillsides? I cast this question more broadly in the section below where I can consider how the genesis and growth of features is embedded in pixel level scores.

### 5.2.1 Shape and scale of incipient features

All the synthetic scenarios presented above used incipient features with square shapes and whose scale was varied using a single parameter, the incipient feature length. The square geometry was useful because squares are oriented in the same way as the regular grids being used, thus imposing a rotational symmetry to translational offsets. However, other rotationally symmetrical shapes could have been used. Figure 8 shows four alternative shapes whose rotational symmetry makes them insensitive to the direction of translational offset between truth and model data. Because these shapes are constrained by their raster representation, it is hard to create different shapes with the same area when objects are small. For the shapes 'square', 'rounded', 'plus', and 'star', all four shapes have approximately equivalent areas (< 3% difference) for shape diameters of 6, 7, 10, and 11 pixels, respectively (Fig. 8A). The number of False Positives and False Negatives to a 1-pixel offset is a function of both the object size and shape (Fig. 8B). As feature objects get larger, the relative error induced by a 1-pixel offset typically



goes down. For a given object area, the relative frequency of error induced by a 1-pixel offset appears to be sensitive to the complexity of object boundaries.

705

To help interpret the relative trade-off between object size and shape, Figure 8C plots the *F1-scores* of the example feature objects in Figure 8A as a function of object area. Due to the symmetry of translational offset, *recall*, *precision*, and *F1-score* are equivalent for this kind of systematic error. Each of these metrics provides a measure of accuracy induced by feature shape alone, independent of the scene-level abundance of features. The error induced by a one-pixel shift between truth and model classification can be directly derived for the square case because of its simple geometry. The number of True Positives is equal to  $l^2 - l$  and the number of False Positives and False Negatives are each equal to  $l$ , where  $l$  is the length of the square in integer units of pixels. Substituting these terms into equation 5 and simplifying yields an equation for *F1-score* specific to square features:

710

$$F1\text{-score}_{sq} = 1 - \frac{l}{l^2} \quad (8)$$

715

The last term in equation 8 explains why accuracy improves as a function of feature area. The area of a square increases faster than its length, thus leading to lower sensitivity to the 1-pixel offset. This ratio is equivalent to the number of pixel edges divided by the total number of pixels for a rasterized shape, which is referred to here as the edge-to-area ratio. The edge-to-area ratio can be calculated for any raster shape and sets how sensitive *F1-score* is to a translational offset. Each kind of shape differs in how the edge-to-area ratio changes as they get larger, thus defining different scaling relationships between accuracy and feature size (Fig. 8C). In general, concave shapes (i.e., ‘square’ and ‘rounded’) are more conducive to higher *F1-scores*. Concavo-convex shapes have more complex boundaries, with some shapes even showing a reduction in accuracy with increasing size (e.g., ‘star’ shape). Even though the synthetic scenarios used in this study assumed square seeds for their incipient features, the coalescing of these incipient shapes into larger objects means that complex boundaries, and thus increasing edge-to-area ratios emerge as feature prevalence increases.

720

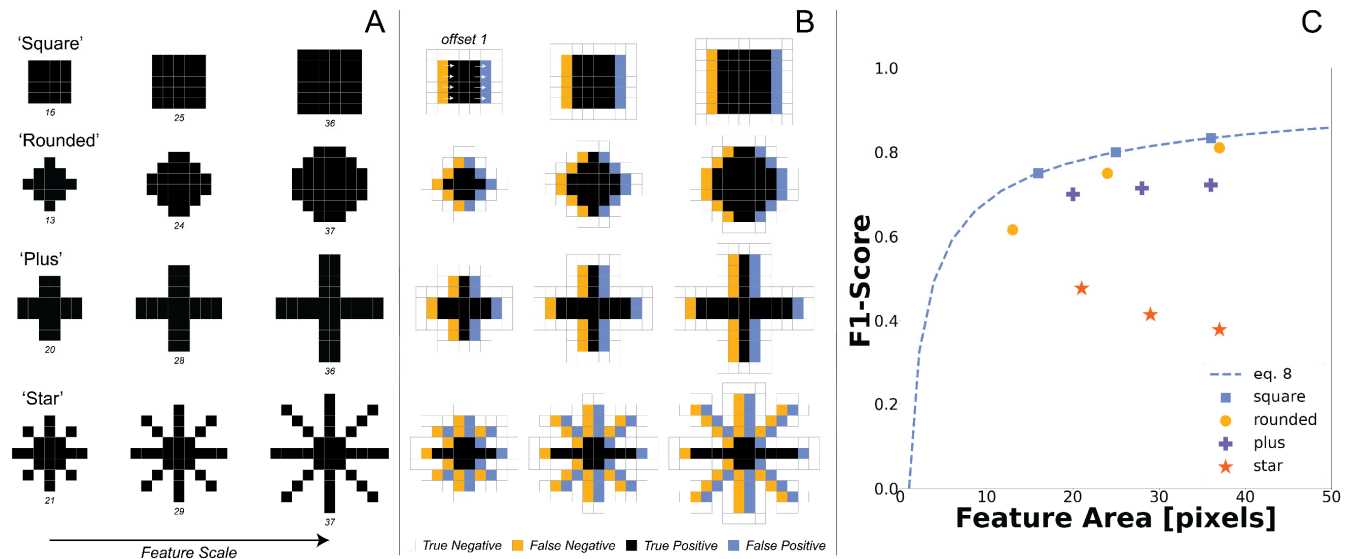
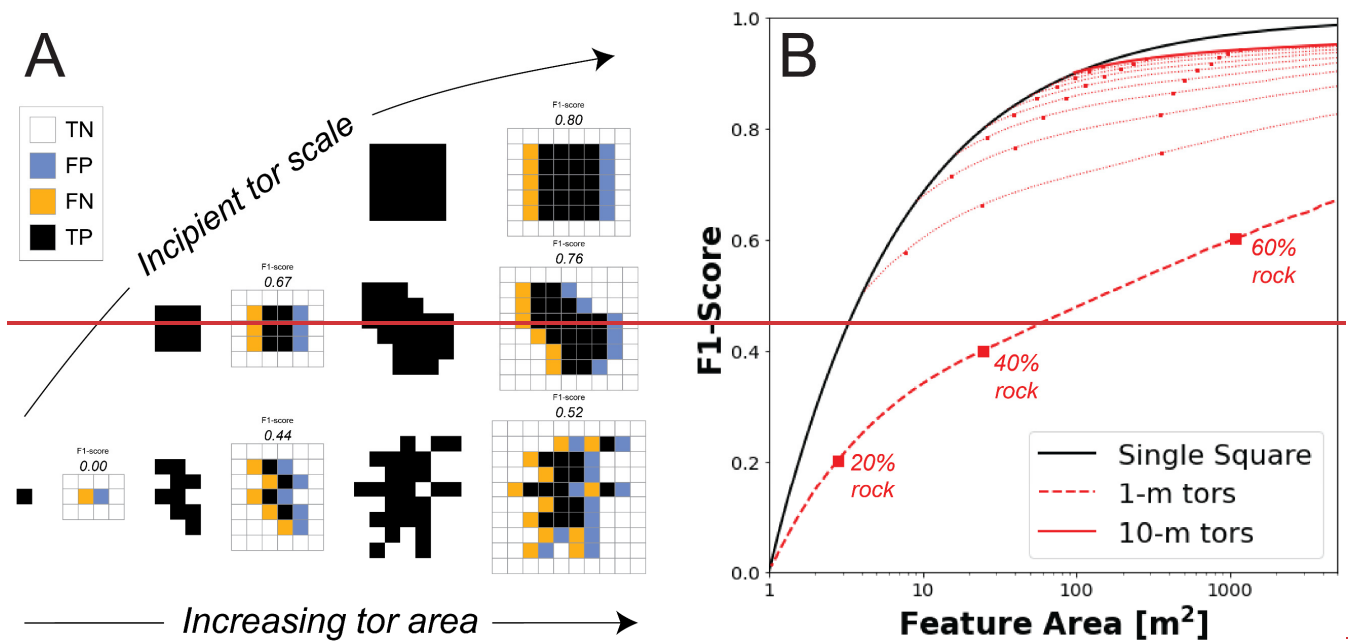


Figure 8: (A) The shape and scale of incipient feature objects directly affects (B) the subsequent frequencies of False Negatives (yellow) and False Positives (blue) to a 1-pixel, translational offset in model classification, (C) which also results in different scaling relationships between object areas and *F1-score*. In A, four different objects are shown that have either convex (i.e., square, rounded) or concavo-convex (i.e., plus, star) boundaries with respect to the matrix. The object area is reported below each shape in pixels. Note that the smallest 'rounded' example is not actually round, but a rotated square. In B, error classes are shown for a 1-pixel shift to the right. Because shapes are all rotationally symmetric with respect to the four cardinal directions, error rates do not depend on the direction of the shift. Only true negatives that share an edge with the other classes



735

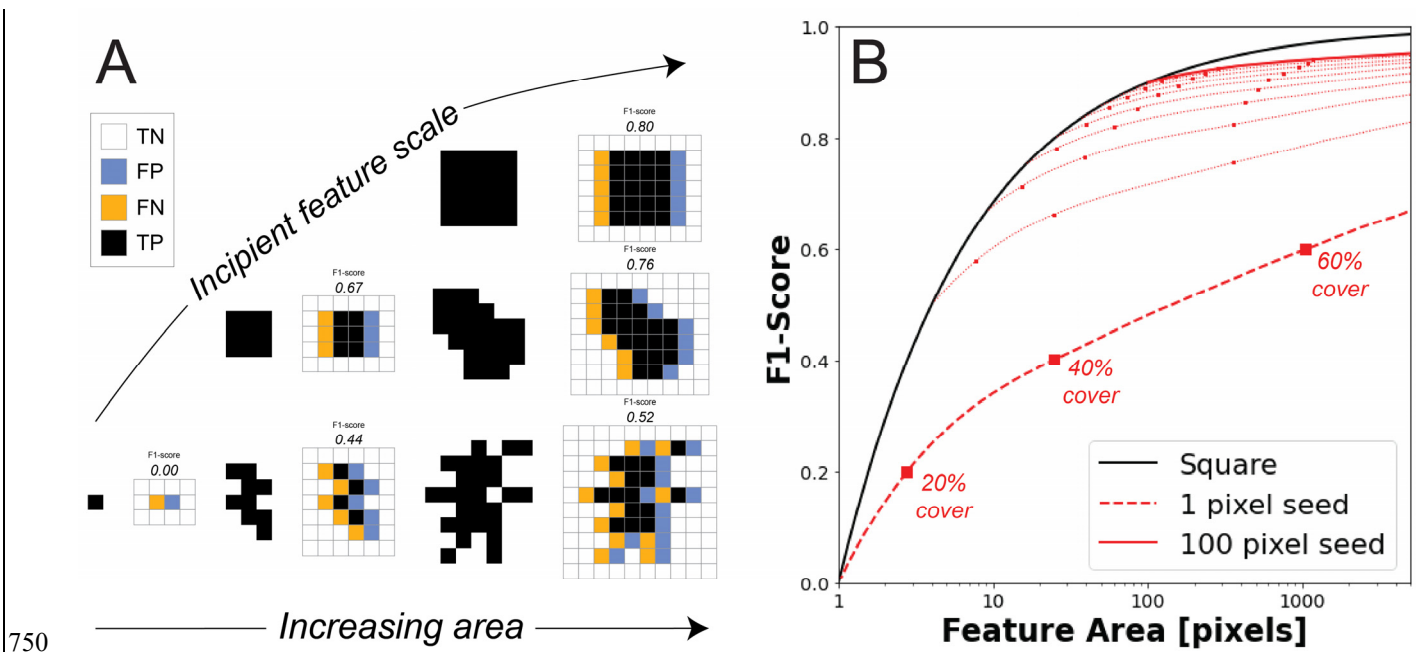
**Figure 7:** The frequency of False Positives and False Negatives (A) is a function of the incipient tor shape and average tor size, which can be quantified for (B) the systematic error scenario using *F1-score*. In A, six permissible tor In C, the *F1-score* for each of the sixteen shapes are plotted as a function of the object area. The function describing how object area and *F1-score* varies for square features (eq. 8) is also plotted as a dashed line for reference.

740

### 5.2.2 Shape and scale of emergent features

In the synthetic scenarios presented above, the minimum feature size is set by the incipient feature length (i.e., 1 to 10 pixels). Because incipient features are placed on the surface randomly, more complex objects are produced where incipient features overlap by chance. To illustrate the implications of this, Figure 9A shows examples of individual objects that can be generated using square seeds. Examples are organized by incipient feature size (rows) and object areas (columns). Adjacent to each object is the error induced by a 1-pixel shift to the right, with its corresponding *F1-score* reported above it. Note that individual objects are not necessarily rotationally symmetric. If an object has a preferred orientation, then error will be enhanced for objects where the long axis is parallel to the translational offset and reduced for objects where the long axis is perpendicular to the translational offset. In practice, the sensitivity of error to object orientation is not realized in the synthetic scenarios above because the random placement of features results in objects without a preferred orientation.

745



750

**Figure 9:** (A) For a given object area, the frequency of False Positives and False Negatives differs among incipient objects and the emergent objects that coalesce from smaller ones, such that (B) *F1-scores* increase with average object area more slowly than square objects do in response to a 1-pixel offset. In A, six permissible object shapes are shown for three different incipient ~~tor~~feature sizes (rows) and three different ~~tor~~object areas (columns). The incipient ~~tor~~feature shape both controls the minimum ~~feature~~scaleobject size and the complexity of ~~feature~~object boundaries, whereby smaller, smaller incipient ~~tor~~features can produce more complex shapes and higher error rates for a given feature size (see associated *F1-scores*). In B, the *F1-score* is plotted as a function of average ~~feature~~object area for all the scenarios shown in Figure 5 (i.e., systematic error only). Square markers indicate scenario (Fig. 5). Markers show values at three bedrock fractions. While average ~~tor~~sizes get different feature fractions. The black line is the function describing how *F1-score* responds to a 1-pixel offset to an individual square object (eq. 8).

755

760

While the examples shown in Figure 9A reiterate the point that error is reduced for larger as more bedrock is exposed, this relationship objects with simpler shapes in response to a 1-pixel offset, it still does not show how object properties are varying in the synthetic scenarios presented above. Figure 9B plots the *F1-score* as a function of the mean object area for the systematic error scenario. To calculate object areas, the binary map of features (i.e., pixel values equal to one) is segmented into objects.

765

Object segmentation is based on adjacency of the target feature class in at least one of its eight neighbours (see examples in Fig. 9A). Objects can contain holes, but these holes do not contribute to their object area. After segmenting the scene into objects, the average object area is calculated and linked to the *F1-scores* reported earlier (Fig. 5). Figure 9B shows that *F1-score* generally improves with increasing object area, albeit in a way that is strongly contingent on the incipient ~~tor~~size. Error at the lowest bedrock fractions largely reflects the error associated with imposed incipient ~~tor~~shape and mediated by the incipient feature size. To illustrate this, the All lines intersect with the function describing *F1-score* for square ~~tor~~s of a given

770

area is also shown for reference (features (eq. 8; solid black line)-) for the limiting case where there is only one object in the scene. For any given incipient feature size though, *F1-score* quickly drops off this function due to the increasing complexity of object boundaries. There is a monotonic increase in *F1-score* with average object area and feature prevalence (markers in

775 Fig. 9B) regardless of the incipient feature size. The scenarios above are not producing shapes like the ‘stars’ shown in Figure  
8. Larger features do lead to high  $FI$ -scores (Fig. 9B). It was already shown that placing larger features in the landscape  
improves accuracy in response translational offset (Figs. 5-6). As such, the negative trends in  $nMCC$  shown in Figures 5B and  
6B suggest that the net result of increasing the size of features, for a given incipient seed, is outweighed by the complexity of  
feature boundaries generated by coalescing them. This analysis suggests that it is paramount to understand the scaling  
properties of features as they become more prevalent to understand how accuracy scores may be affected by small co-  
780 registration errors. Finally, the sensitivity of accuracy metrics to the size and shape of individual features begs important  
questions as to how stable accuracy metrics are to increasing spatial resolution. As airborne remote sensing is supplemented  
and superseded by drone-based mapping, there is good reason to believe that the shapes and scales of better resolved features  
may change, and thus influence how binary classifiers perform.

### **6.3 Other geomorphic applications**

#### **5.3 Recommendations and future directions**

785 Many geomorphic tasks share the need for binary classifiers that perform well across gradients in feature abundance. Whether  
constraining the density of landslide scars, ~~river channels~~channel erosion, bedrock outcrops, or pit-mound features, geomorphic  
studies often rely on fine-scale mapping to determine how feature size, extent, and prevalence respond to differences in  
environmental forcing. ~~As such, there is a general need for classifiers that successfully handle imbalanced data. In all the~~  
~~synthetic scenarios presented here, increased target class density was generated by randomly distributing the nuclei of incipient~~  
~~790 features within the model domain. This is perhaps a reasonable analogue to the case where bedrock tors are exhumed from a~~  
~~spatially random distribution of somewhat more resistant bedrock (e.g., due to differences in chemical composition, fracture~~  
~~density, etc.) that underly thin soils near denudational thresholds. In contrast, many topographic features show striking~~  
~~evidence for self-organization (Hallet, 1990; Phillips, 1999; Murray et al., 2009) where feature properties instead reflect~~  
~~interactions of local positive feedbacks and far field negative feedbacks (e.g., Gabet et al., 2014). Unlike the synthetic surfaces~~  
~~795 shown here, the emergence of patterned topography and the regular spacing of features will maintain isolation of features even~~  
~~at very high densities. In such cases, we might expect the shape and size of features to follow well defined scaling laws that~~  
~~respond quite differently to systematic error. There is a general need for classifiers that successfully handle imbalanced data.~~  
This paper set out to understand how two widely used pixel-level accuracy metrics perform across gradients in feature  
prevalence. By using synthetic examples where the error structure of the data is known, heuristics can be developed for best  
800 practices when the research design specifically calibrates and validates binary classifiers across gradients in feature abundance.  
Four key recommendations emerged:

~~It is beyond the scope of this analysis to test the variety of scaling relationships that different topographic features exhibit in~~  
~~nature. That said, this analysis emphasizes the importance of understanding how feature size and shape covary with each other~~

805 as feature density increases. If scaling relationships do exist for a given type of feature and are known, then they provide the  
baseline for interpreting how and whether pixel-level accuracy scores are differentially sensitive to feature abundance. Even  
though pixel level metrics like *MCC* and *nMCC* handle imbalanced data well and address the challenge of asymmetry with  
respect to target class, the examples shown here suggest that it should not be assumed that these pixel-level metrics will be  
invariant as a function of feature abundance. How pixel level metrics vary under different error scenarios need to be modelled  
810 explicitly so that trends in accuracy can be interpreted. The approach taken here was to use synthetic feature maps to yield  
insight into how pixel level scores relate to scene level attributes (sp., bedrock fraction). Future work would benefit from using  
landscape evolution models to inform how pixel level scores are expected to vary under different error scenarios for the  
relevant geomorphic processes at play. As numerical models of the land surface attempt to keep pace with increasingly higher  
resolution, process scale observations (Tucker & Hancock, 2010), they have the potential to provide hypothesis driven  
815 statistical analysis for how pixel level accuracy scores should vary with feature abundance for different types of error.

In many cases, we expect error to depend on the topographic proxy being used (e.g., slope, curvature, roughness) such that  
error may be higher in scenes closer to the feature detection limit (i.e., where fewer features are observed). As such, more  
careful consideration of spatial autocorrelation in error and the subsequent trends in accuracy scores that arise is needed.  
820 Further attention to this issue will undoubtedly reveal different relationships between pixel level scores and scene level  
attributes than those presented here. Nevertheless, the error scenarios considered reveal that the domain over which *nMCC* is  
expected to be comparable across scenes can be quite limited depending on the source of error, the error rate, and the size and  
shape of features being assessed.

(1) Matthews Correlation Coefficient, and its normalized equivalent (*nMCC*), are much better suited than *FI-score* to  
825 comparing accuracy scores when feature abundances vary across classified scenes. Even after addressing the problem  
of asymmetry, macro *FI-score* tends to over-penalize random error.

(2) For random error, caution is warranted in interpreting *nMCC* near the endmember cases of zero and full feature  
830 coverage because random error preferentially modifies the dominant class. Though scores are relatively invariant  
only between ~20-80% feature coverage, this domain might be expanded for scenes with more heterogeneous feature  
distributions.

(3) For systematic error, *nMCC* is strongly sensitive to the size and shape of individual objects. Larger objects with  
835 simpler boundaries are less sensitive to this kind of error because their edge-to-area ratios are small. As such, it is  
important to characterize both co-registration uncertainty and the attributes of the individual objects being mapped.

(4) Before training and testing classifiers on imbalanced data, it is essential to establish baseline expectations for how pixel-level accuracy scores respond to potential sources of error over the range of feature abundances used. This can be accomplished through numerical simulation.

840

Simulating a suite of simple scenarios with a known error structure and uniform incipient seeds provided some insight into how pixel-level accuracy metrics behave across gradients in feature prevalence. Real-world applications are decidedly more complex. In the scenarios presented here, increased feature density was simulated by randomly distributing the nuclei of incipient features within the model domain. Such a treatment may be relevant to some applications but is clearly limited. Figure 1 anticipated three clear limitations of simulating features in this way. Many features show evidence for: a characteristic scale and spacing (e.g., mima mounds in Fig. 1A), size distributions spread across a wide range of scales (e.g., bedrock exposure in Fig. 1B), and anisotropy (e.g., gully erosion in Fig. 1C). As such, more work is needed to understand how pixel-level accuracy metrics perform on imbalanced data that exhibit these properties. To this end, three promising future research directions are:

845

850

(1) As **landscape evolution modelling** attempts to keep pace with increasingly higher resolution observations (Tucker & Hancock, 2010), it also has wide potential for error analysis. Instead of randomly generating features, numerical models can produce more realistic feature distributions that are derived from the relevant geomorphic transport laws at play (Dietrich et al., 2003). A process-based approach towards error assessment could be used to identify under what conditions binary classifiers can be reliably compared across gradients in feature fraction.

855

(2) Pixel-level accuracy scores are built on the confusion matrix, which does not retain the **spatial autocorrelation** structure or the **semantic content** of feature objects. Given the importance of the size and shape of features to some error scenarios, the path forward may lie in multi-scale, object-based image analysis (e.g., Drăguț and Eisank, 2011). Object-based image analysis is on the cutting edge of feature extraction from remote sensing data (Hossain and Chen, 2019). How to reliably evaluate the accuracy of image segmentation algorithms though requires creative re-thinking and re-tooling of standard pixel-level accuracy scores (Cai et al., 2018).

860

(3) Both opportunities above emphasize the over-arching challenge of the rapidly changing landscape of increasing **spatial resolution** data. Higher resolution data both impacts the practical challenge of co-registration error as well as highlights the more theoretical challenge of semantic vagueness, or the notion that feature boundaries may not be sharply defined (Sofia, 2020). As data resolution increases, traditional methods in image segmentation and binary classification may require new approaches (Zheng and Chen, 2023).

865

On the one hand, this paper is a call to action on adopting standard methods from the data sciences into surface processes research. On the other hand, geomorphic questions provide a diversity of real-world use-cases where these ‘standard’ methods

870

can be put to the test and new methods can be developed. As machine learning approaches towards geomorphic mapping proliferate, a better understanding is needed on how these methods will perform on the scientific tasks that are driving surface processes research forward.

## 6 Conclusions

875 ~~With increasing access to high resolution data and increasing focus on fine scale mapping of topographic features, pixel~~Pixel-level accuracy assessment provides a powerful tool for understanding how well classifiers built from ~~high resolution~~high resolution topography are performing. To be most useful, the limitations of commonly used metrics like *precision*, *recall*, and *F1-score* need to be considered. Classification tasks that span large gradients in feature abundance are particularly vulnerable to biases in these metrics because data is ~~strongly~~imbalanced and the choice of target class matters. More robust metrics like *MCC* and  
880 *nMCC* largely address these methodological challenges. However, caution is still warranted in comparing pixel-level scores across gradients in feature density and extent (~~e.g., bedrock fraction~~). If error is random and uniform across scenes, then *nMCC* will dramatically worsen near endmember cases because the more prevalent class ~~will be~~is preferentially modified, ~~though~~  
885 ~~this effect may be mediated by pooling data from many different scenes~~. If the model is systematically offset from the truth grid, then an asymmetrical sensitivity of *nMCC* can arise depending on ~~the~~ assumptions for the genesis and growth of individual features. As the size of individual features increases ~~with feature abundance~~, there ~~will also be~~is lower sensitivity to systematic offset. However, if the shapes of features are also getting more complex, then the increased edge to area ratio of individual features can counteract and exceed improvements in accuracy associated with larger feature sizes. Though pixel-level metrics used in the machine learning and remote sensing community should be more widely adopted in geomorphic research, further work is needed to understand how different sources of error ~~might~~ decouple pixel-level from scene-level  
890 measures of accuracy.

### Appendix A: Random error and accuracy metrics

Section 5.1 reported how pixel-level accuracy scores vary as a function of bedrock fraction for a fixed rate of random error. While the synthetic surfaces were generated using Python, the results shown in Figure 4 can be directly derived from the mean random error rate ( $\bar{e}_r$ ) and true ~~bedrock~~feature fraction ( $f_B f_f$ ) analytically. Under this scenario, the probability of flipping  
895 either class is independent of the prevalence and location of ~~bedrock~~outeropsfeatures such we can define the average frequencies for all four components of the confusion matrix. The relative frequencies of each outcome are the product of the average rate of error (or non-error) and the average abundance of the true class. For example, the True Positives reflect both the probability of ~~bedrock~~the feature occurring ( $f_B f_f$ ) and the probability of not being flipped in the model due to random error (i.e.,  $1 - \bar{e}_r$ ). The frequencies of all four classification outcomes are:



900

$$f_{TP} = (1 - \bar{e}_r) f_b f_f$$

(A1)

$$f_{FP} = \bar{e}_r f_b f_f$$

(A2)

$$f_{FN} = \bar{e}_r (1 - f_b) (1 - f_f)$$

(A3)

905

$$f_{TN} = (1 - \bar{e}_r) (1 - f_b) (1 - f_f)$$

(A4)

Because we also know that the bedrockfraction fraction in the model ( $f_{\text{BMM}} f_m$ ) must equal the sum of the fractions of True Positives and False Negatives, these equations yield the relationship:

910

$$f_{\text{BMM}} f_m = (1 - \bar{e}_r) f_b f_f + \bar{e}_r (1 - f_b) (1 - f_f)$$

(A5)

Equation A5 can be rearranged and simplified to describe how the model bedrockfraction fraction and is related to the true bedrockfraction fraction vary as a linear function of the random error rate:

915

$$f_{\text{BMM}} f_m = (1 - 2\bar{e}_r) f_b f_f + \bar{e}_r$$

(A6)

The relationships shown in Figure 4A (main text) are equivalent to equation A6 for different error rates. That the Python-generated scenes match the analytical solution indicates that the domain used for these synthetic scenes is large enough to adequately sample population statistics. Note that equation A6 provides a prediction for the relationship between true and model bedrock fractions only if error is uniform and random across scenes. In such cases, the average error rate can be directly inferred from both the slope and y-intercept of the regression. ~~If this reasoning is flipped, then empirical studies using scene-level regressions (DiBiase et al., 2012; Rossi et al., 2020) provide prima facie evidence for whether classification error is random and uniform across scenes. For example, while all regressions reported in Rossi et al. (2020) were forced through the origin, the best fit linear regressions yielded negative y-intercepts suggesting that error rates were systematically higher at lower bedrock fractions.~~

925

Because pixel-level accuracy scores can be derived directly from the confusion matrix, the simplified assumptions of random, uniform error also facilitate prediction for how *F1-score* and *nMCC* will vary with the true bedrockfraction fraction. Substituting the values from eqs. A1-A4 into equation 5 (main text) yields:

930

$$F1\text{-score} = \frac{2f_b(1-\bar{e}_r)}{2f_b(1-\bar{e}_r) + \bar{e}_r} \frac{2f_f(1-\bar{e}_r)}{2f_f(1-\bar{e}_r) + \bar{e}_r}$$

(A7)

which is equivalent to the numerically generated black curves in Figure 4B. Similarly, substituting eqs. A1-A4 into equation 6 (main text) yields:

$$MCC =$$

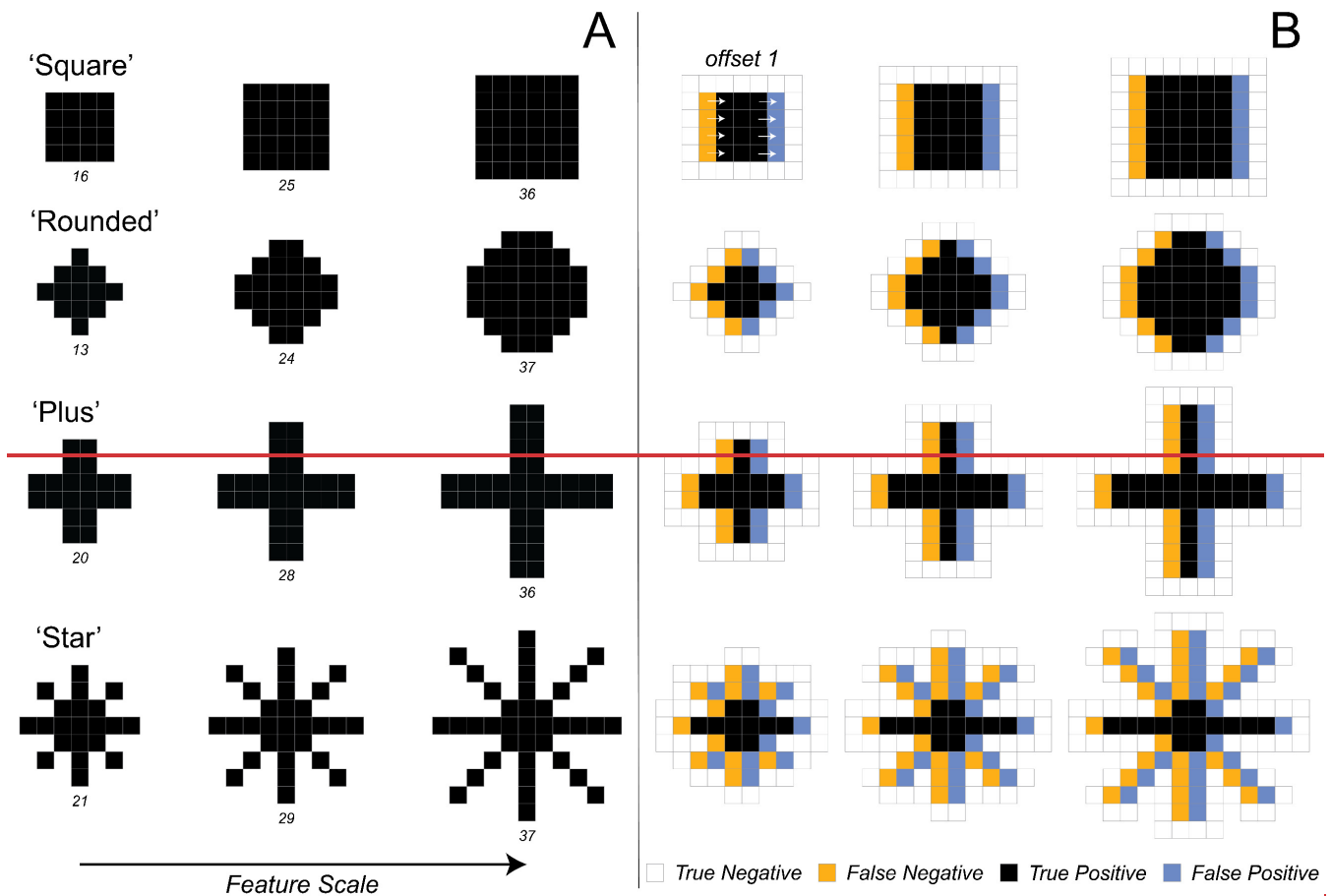
$$\frac{\sqrt{f_b} \times \sqrt{1-f_b} \times (1-2\bar{e}_r)}{\sqrt{f_b + \bar{e}_r - \bar{e}_r^2 - f_b^2 - 4\bar{e}_r f_b - 4\bar{e}_r^2 f_b^2}} \frac{\sqrt{f_f} \times \sqrt{1-f_f} \times (1-2\bar{e}_r)}{\sqrt{f_f + \bar{e}_r - \bar{e}_r^2 - f_f^2 - 4\bar{e}_r f_f - 4\bar{e}_r^2 f_f^2}}$$

$$(A8)$$

which is equivalent to the numerically generated red curves in Figure 4B. Though the expression for  $MCC$  under random, uniform error is complex, it reveals why there is strong and symmetrical sensitivity near the endmember cases of zero and all bedrock. The numerator in eq. A8 decreases faster than the denominator near endmember cases regardless of the average error rate. Since  $f_b f_f$  and  $1 - f_b f_f$  are complementary and  $\bar{e}_r$  is assumed to be constant, this reduction in  $MCC$  is also symmetrical around an optimal bedrock fraction of 0.5.

### Appendix B: Feature shape and systematic error

In this analysis, bedrock tors are treated as square features whose scale is varied with a single parameter, the ‘tor’ length. The square geometry is useful because it is oriented in the same way as the regular grid over which the synthetic landscapes are generated. The random placement of incipient tors on the surface ensures that bedrock features do not have a preferential orientation and translational errors do not depend on the orientation of offset. While relaxing these assumptions are beyond the scope of this study, it is worth probing more deeply on how tors are simulated to help explain the asymmetrical sensitivity of  $nMCC$  to bedrock fraction when the model data is systematically offset from truth (Figs. 5-6). Specifically, I show in this appendix how the frequency of False Positives and False Negatives are linked to the shape and size of features. Both the incipient tor shape and the subsequent aggregation of these shapes into larger bedrock features are what set the overall error rate. By incipient tor shape, I am referring to the seed shape used to generate bedrock from the random placement of tor centres. While I only used a square seed in the main analysis, Figure B1 shows the importance of seed shape to generating false positives and false negatives when the truth and model features are systematically offset by one pixel. In Figure B1A, I show four shapes at three different spatial scales. Because seed shapes are constrained by their raster representation, it is hard to create different shapes with the same area when the seed shape is small. For the shapes ‘square’, ‘rounded’, ‘plus’, and ‘star’, the shape area is approximately equivalent for shape diameters of 6, 7, 10, and 11 pixels, respectively. For these radially symmetrical shapes, a 1-pixel shift produces the same number of false positives and false negatives regardless of the orientation of the shift.



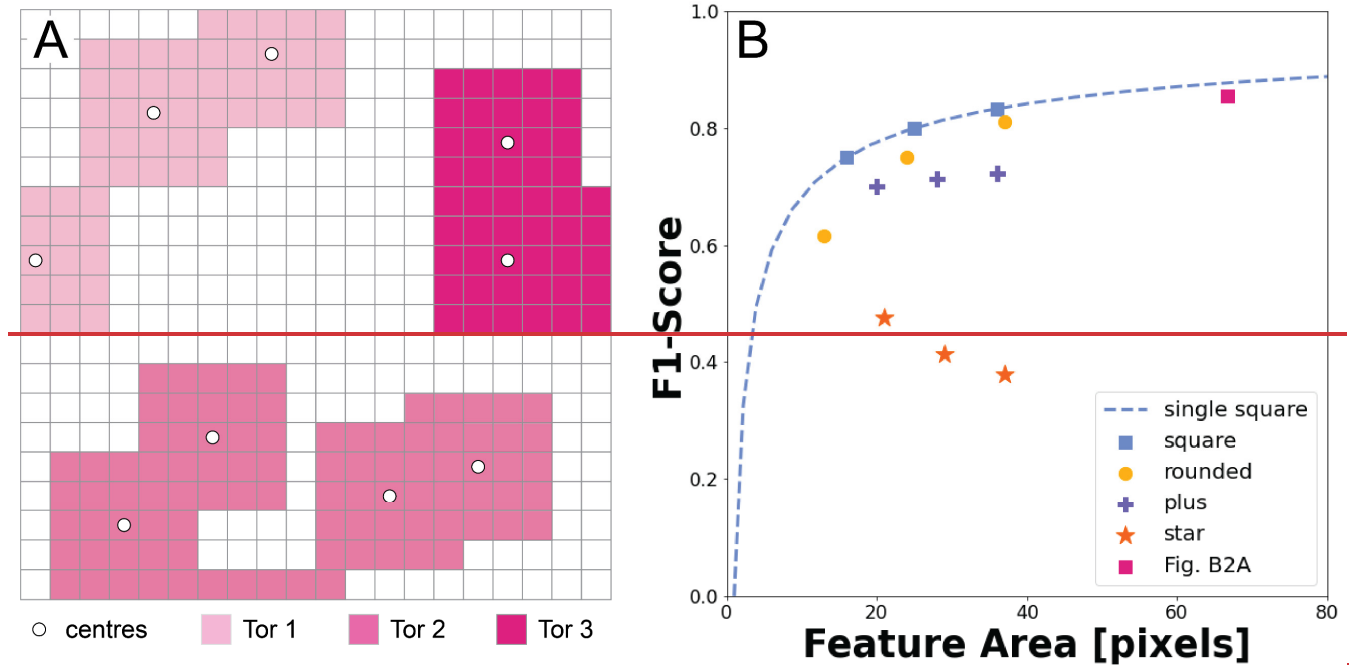
960 **Figure B1:** (A) Shape and scale of incipient tors directly affects (B) the subsequent frequencies of False Negatives (yellow) and False Positives (blue) to a translational offset in model classification. In A, four different feature shapes are shown that have either convex (i.e., square, rounded) or concavo-convex (i.e., plus, star) boundaries with respect to the soil matrix. The feature area is reported below each shape in pixels. Note that the smallest 'rounded' example is not actually round, but a rotated square. As features get too small with respect to the data resolution, it becomes difficult to represent complex objects using a regular, square grid. In B, error classes are shown for a 1-pixel shift to the right. Because shapes are all rotationally symmetric with respect to the four cardinal directions, error rates do not depend on the direction of the shift. Only true negatives that share an edge with the other classes are shown.

970 While much of the analysis has emphasized that  $MCC$  and  $nMCC$  are superior to  $F1$  score for accuracy assessment when True Negatives matter,  $F1$  score is well suited to the task of isolating how feature size and shape impact error independent of bedrock fraction. The geometry of an individual square tor is a useful starting point because the error induced by a one-pixel shift between truth and model classification is readily derived from its simple geometry. The number of True Positives is equal to  $l^2 - l$  and the number of False Positives and False Negatives are each equal to  $l$ , where  $l$  is the length of the square. Substituting these terms into eq. 5 (main text) and simplifying yields an equation for  $F1$  score specific to square features:

$$F1\ score_{sq} = 1 - \frac{l}{l^2} \quad (B1)$$

Because the area of a square increases faster than its length, the last term in equation B1 explains why accuracy improves as a function of feature area. To extend this further, I also compare how the different shapes shown in Figure B1 impact  $F1$  scores (Fig. B2B). The key property that is changing for these different shapes is the edge to area ratio, whereby concave shapes (i.e., ‘square’ and ‘rounded’) are generally more conducive to higher  $F1$  scores. However, the size of features is also very important. In all but the ‘star’ example,  $F1$  scores improve as features get larger. The ‘star’ does not follow the pattern because it is the only example here where the edge to area ratio increases with feature size.

975



980 **Figure B2:** (A) Example bedrock map like those produced in this analysis and (B) the relationship between feature area and  $F1$  score. In A, nine ‘tor’ centres produce three individual tors. In B, the  $F1$  score in A is plotted as a function of the average feature area alongside the seed shapes shown in Figure B1. For reference, I also plot the function describing how area and  $F1$  score vary for square tors. Note that even though the bedrock map shown in A is generated using randomly distributed square outerops, the  $F1$  score is lower than the dashed blue line due to the more complex boundaries generated by coalescing incipient tors into a fewer number of features.

985 This feature level assessment provides further insight into why Figures 5–6 (main text) show positive trends in  $F1$  score and negative trends in  $nMCC$  as a function of bedrock fraction. Increasing feature size favours lower error while increasing feature complexity favours higher error. Figure 7 (main text) demonstrates that the net result of these competing effects is monotonic increases in  $F1$  score as a function of bedrock fraction, all other things being equal. This is because it is difficult to overcome the strong sensitivity of  $F1$  score to how balanced the data are. Instead,  $nMCC$  reveals that the impact of increasing complexity of feature shape slightly outweighs the increase in feature size leading to a modest negative relationship to bedrock fraction (Fig. 5 main text).

990

## Data Availability

995 ~~Figures~~Figure 1- elevation data was downloaded from OpenTopography (2010 Channel Islands Lidar Collection, 2012; Anderson et al., 2012; Reed, 2006). Figure 2 and Table 1 are based on the bedrock mapping at site P4P01 from Rossi et al. (2020). Maps for 1-m truth and model data at this site can be accessed at [https://github.com/mwrossi/cfr\\_extremes](https://github.com/mwrossi/cfr_extremes). These classified maps are based on 2018 Pictometry® orthomosaicked air photos purchased by Boulder County and airborne lidar data acquired by the National Center for Airborne Laser Mapping for the Boulder Creek Critical Zone Observatory (Anderson et al., 2012). Synthetic surfaces presented in Figures 3-79 were built in Python. Scripts can be accessed at <https://github.com/mwrossi/bedrock-mapping-accuracy>~~https://github.com/mwrossi/feature-mapping-accuracy~~. Once through 1000 review, the main code will continue to be hosted on Github, but scripts and files used for generating ~~figures~~each figure will be archived on Figshare.

## Competing interests

The author declares that there is no conflict of interest.

## Acknowledgements

1005 This project was supported by funding from the Geomorphology and Land-Use Dynamics Program at the National Science Foundation (EAR-1822062) and benefited from discussions with Bob Anderson, Suzanne Anderson, Roman DiBiase, Brittany Selander, and Greg Tucker. The author thanks one anonymous reviewer and Stuart Grieve for their thoughtful and constructive reviews.

## References

1010 2010 Channel Islands Lidar Collection, United States Geological Survey, distributed by OpenTopography [data set], <https://doi.org/10.5069/G95D8PS7>, 2012.

1015 Ågren, A. M., Larson, J., Paul, S. S., Laudon, H., and Lidberg, W.: Use of multiple LIDAR-derived digital terrain indices and machine learning for high-resolution national-scale soil moisture mapping of the Swedish forest landscape, *Geoderma*, 404, 115280, <https://doi.org/10.1016/J.GEODERMA.2021.115280>, 2021.

~~Anderson, R. S.: Modeling the tor dotted crests, bedrock edges, and parabolic profiles of high alpine surfaces of the Wind River Range, Wyoming, *Geomorphology*, 46, 35–58, [https://doi.org/10.1016/S0169-555X\(02\)00053-3](https://doi.org/10.1016/S0169-555X(02)00053-3), 2002.~~

- 1020 Anderson, S.P., Qinghua, G., and Parrish, E.G.: Snow-on and snow-off Lidar point cloud data and digital elevation models for study of topography, snow, ecosystems and environmental change at Boulder Creek Critical Zone Observatory, Colorado, National Center for Airborne Laser Mapping—~~[data set], <https://doi.org/10.5069/G93R0QR0>~~, distributed by OpenTopography ~~[data set], <https://doi.org/10.5069/G93R0QR0>~~, 2012.
- 1025 ~~Andrews, D. J. and Bucknam, R. C.: Fitting degradation of shoreline scarps by a nonlinear diffusion model, *J. Geophys. Res. Solid Earth*, **92**, 12857–12867, <https://doi.org/10.1029/JB092IB12P12857>, 1987.~~
- Baldi, P., Brunak, S., Chauvin, Y., Andersen, C. A. F., and Nielsen, H.: Assessing the accuracy of prediction algorithms for classification: an overview, *Bioinformatics*, **16**, 412–424, <https://doi.org/10.1093/BIOINFORMATICS/16.5.412>, 2000.
- 1030 ~~Barnhart, K. R., Tucker, G. E., Doty, S. G., Glade, R. C., Shobe, C. M., Rossi, M.W., and Hill, M. C.: Projections of landscape evolution on a 10,000 year timescale with assessment and partitioning of uncertainty sources, *J. Geophys. Res.-Earth*, **125**, e2020JF005795, <https://doi.org/10.1029/2020JF005795>, 2020.~~
- 1035 Bertin, S., Jaud, M., and Delacourt, C.: Assessing DEM quality and minimizing registration error in repeated geomorphic surveys with multi-temporal ground truths of invariant features: Application to a long-term dataset of beach topography and nearshore bathymetry, *Earth Surf. Process. Landforms*, **47**, 2950-2971, <https://doi.org/10.1002/ESP.5436>, 2022.
- ~~Bunn, M. D., Leshchinsky, B. A., Olsen, M. J., and Booth, A.: A simplified, object-based framework for efficient landslide inventorying using LIDAR digital elevation model derivatives, *Remote Sens.*, **11**, 303, <https://doi.org/10.3390/rs11030303>, 2019.~~
- ~~Cai, L., Shi, W., Miao, Z., and Hao, M.: Accuracy assessment measures for object extraction from remote sensing images, *Remote Sens.*, **10**, 303, <https://doi.org/10.3390/rs10020303>, 2018.~~
- 1045 Chicco, D. and Jurman, G.: The advantages of the Matthews correlation coefficient (MCC) over F1 score and accuracy in binary classification evaluation, *BMC Genomics*, **21**, 1-13, <https://doi.org/10.1186/S12864-019-6413-7>, 2020.
- ~~Chicco, D., Warrens, M. J., and Jurman, G.: The Matthews Correlation Coefficient (MCC) is More Informative Than Cohen's Kappa and Brier Score in Binary Classification Assessment, *IEEE Access*, **9**, 78368–78381, <https://doi.org/10.1109/ACCESS.2021.3084050>, 2021a.~~
- 1050

- Chicco, D., Tötsch, N., and Jurman, G.: The ~~matthews~~Matthews correlation coefficient (~~Mee~~MCC) is more reliable than balanced accuracy, bookmaker informedness, and markedness in two-class confusion matrix evaluation, *BioData Min.*, 14, 1–22, <https://doi.org/10.1186/S13040-021-00244-Z>, ~~2021a~~2021b.
- ~~Chicco, D., Warrens, M. J., and Jurman, G.: The Matthews Correlation Coefficient (MCC) is More Informative Than Cohen's Kappa and Brier Score in Binary Classification Assessment, IEEE Access, 9, 78368–78381, https://doi.org/10.1109/ACCESS.2021.3084050, 2021b.~~
- Chinchor, N.: MUC-4 evaluation metrics, in: Proceedings of MUC-4 - the 4th Conference on Message Understanding, ~~1992-McLean, VA, 16-18 June 1992, 22-29, https://doi.org/10.3115/1072064.1072067, 1992.~~
- Clubb, F. J., Mudd, S. M., Milodowski, D. T., Hurst, M. D., and Slater, L. J.: Objective extraction of channel heads from high-resolution topographic data, *Water Resour. Res.*, 50, 4283–4304, <https://doi.org/10.1002/2013WR015167>, 2014.
- ~~Culling, W. E. H.: Soil Creep and the Development of Hillside Slopes, 71, 127–161, https://doi.org/10.1086/626891, 2015.~~
- Cunningham, D., Grebby, S., Tansey, K., Gosar, A., and Kastelic, V.: Application of airborne LiDAR to mapping seismogenic faults in forested mountainous terrain, southeastern Alps, Slovenia, *Geophys. Res. Lett.*, 33, <https://doi.org/10.1029/2006GL027014>, 2006.
- ~~Davies, A. B., Levick, S. R., Asner, G. P., Robertson, M. P., Van Rensburg, B. J., Parr, C. L., Davies, A. B., Robertson, M. P., and Van Rensburg, B. J.: Spatial variability and abiotic determinants of termite mounds throughout a savanna catchment, Ecography, 37, 852–862, https://doi.org/10.1111/ecog.00532, 2014.~~
- DiBiase, R. A., Heimsath, A. M., and Whipple, K. X.: Hillslope response to tectonic forcing in threshold landscapes, *Earth Surf. Process. Landforms*, 37, 855–865, <https://doi.org/10.1002/ESPesp.3205>, 2012.
- Dietrich, W. E., Bellugi, D. G., Sklar, L. S., Stock, J. D., Heimsath, A. M., and Roering, J. J.: Geomorphic Transport Laws for Predicting Landscape form and Dynamics, *Geophys. Monogr. Ser.*, 135, 103–132, <https://doi.org/10.1029/135GM09>, 2003.
- Doane, T. H., ~~Edmonds, D.~~, Yanites, B. J., ~~Edmonds, D. A.~~, and ~~Lewis, Q.~~: ~~Topographic Roughness on Forested Hillslopes: A Theoretical Approach for Quantifying~~Novick, K. A.: Hillslope Sediment Flux From Tree Throw, Geophys. Res. Lett., 48, roughness reveals forest sensitivity to extreme winds, Proc. Natl. Acad. Sci. U. S. A., 120, e2212105120, https://doi.org/10.1029/2021GL094987, 2021+1073/PNAS.2212105120, 2023.

- 1090 ~~Fraser, O. L., Bailey, S. W., Ducey, M., Drăgut, L. and Eisank, C.: Object representations at multiple scales from digital elevation models, *Geomorphology*, 129, 183-189, <https://doi.org/10.1016/j.geomorph.2011.03.003>, 2011.~~
- ~~Hossain, M. J., and McGuire, K. J.: Predictive modeling of bedrock outcrops and associated shallow soil in upland glaciated landscapes, *Geoderma*, 376, 114495, <https://doi.org/10.1016/J.GEODERMA.2020.114495>, 2020.~~
- 1095 ~~Gabet, E. J., Perron, J. T., and Johnson, D. L.: Biotic origin and Chen, D.: Segmentation for Mima mounds supported by numerical modeling, 206, 58–66 *Object-Based Image Analysis (OBIA): A review of algorithms and challenges from remote sensing perspective*, *ISPRS J. Photogramm.*, 150, 115-134, <https://doi.org/10.1016/J.GEOMORPH.2013.09.018>, 2014.~~
- ~~Gilbert, G. K.: The Convexity of Hilltops, 17, 344–350, <https://doi.org/10.1086/621620>, 1909.~~
- 1100 ~~Hallet, B.: Spatial self-organization in geomorphology: from periodic bedforms and patterned ground to scale-invariant topography, *Earth Science Rev.*, 29, 57–75, [https://doi.org/10.1016/0012-8252\(0\)90028-T](https://doi.org/10.1016/0012-8252(0)90028-T), 1990.~~
- ~~Heimsath, A. M., DiBiase, R. A., and Whipple, K. X.: Soil production limits and the transition to bedrock dominated landscapes, *Nat. Geosci.*, 5, 210–214, <https://doi.org/10.1038/ngeo1380>, 2012.~~
- 1105 ~~Heimsath, A. M., Dietrich, W. E., Nishiizumi, K., and Finkel, R. C.: The soil production function and landscape equilibrium, *Nat.*, 388, 358–361, <https://doi.org/10.1038/41056>, 1997 *j.isprs/jprs.2019.02.009*, 2019.~~
- ~~Jaboyedoff, M., Oppikofer, T., Abellán, A., Derron, M. H., Loye, A., Metzger, R., and Pedrazzini, A.: Use of LIDAR in landslide investigations: A review, *Nat. Hazards*, 61, 5–28, <https://doi.org/10.1007/S11069-010-9634-2> **FIGURES/9**, 2012.~~
- ~~Korzeniowska, K., Pfeifer, N., and Landtwing, S.: Mapping gullies, dunes, lava fields, and landslides via surface roughness, *Geomorphology*, 301, 53-67, <https://doi.org/10.1016/j.geomorph.2017.10.011>, 2018.~~
- 1115 ~~Levick, S. R., Asner, G. P., Chadwick, O. A., Khomo, L. M., Rogers, K. H., Hartshorn, A. S., Kennedy-Bowdoin, T., and Knapp, D. E.: Regional insight into savanna hydrogeomorphology from termite mounds, *Nat. Commun.*, 1, ~~4–765~~, <https://doi.org/10.1038/ncomms1066>, 2010.~~



1120 ~~Marshall, J. A. and Roering, J. J.: Diagenetic variation in the Oregon Coast Range: Implications for rock strength, soil  
production, hillslope form, and landscape evolution, J. Geophys. Res. Earth Surf., 119, 1395–1417,  
https://doi.org/10.1002/2013JF003004, 2014.~~

1125 Matthews, B. W.: Comparison of the predicted and observed secondary structure of T4 phage lysozyme, *Biochim. Biophys.  
Acta - Protein Struct.*, 405, 442–451, [https://doi.org/10.1016/0005-2795\(75\)90109-9](https://doi.org/10.1016/0005-2795(75)90109-9), 1975.

Milodowski, D. T., Mudd, S. M., and Mitchard, E. T. A.: Topographic roughness as a signature of the emergence of bedrock  
in eroding landscapes, *Earth Surf. Dyn.*, 3, 483–499, <https://doi.org/10.5194/ESURF-3-483-2015>, 2015.

1130 Morell, K. D., Regalla, C., Leonard, L. J., Amos, C., and Levson, V.: Quaternary rupture of a crustal fault beneath Victoria,  
British Columbia, Canada, *GSA Today*, 27, 4–10, <https://doi.org/10.1130/GSATG291A.1>, 2015.

~~Murray, A. B., Lazarus, E., Ashton, A., Baas, A., Coco, G., Coulthard, T., Fonstad, M., Haff, P., McNamara, D., Paola, C.,  
Pelletier, J., and Reinhardt, L.: Geomorphology, complexity, and the emerging science of the Earth's surface, 103, 496–505,  
<https://doi.org/10.1016/J.GEOMORPH.2008.08.013>, 2009.~~

1135 Passalacqua, P., Belmont, P., Staley, D. M., Simley, J. D., Arrowsmith, J. R., Bode, C. A., Crosby, C., DeLong, S. B., Glenn,  
N. F., Kelly, S. A., Lague, D., Sangireddy, H., Schaffrath, K., Tarboton, D. G., Wasklewicz, T., and Wheaton, J. M.: Analyzing  
high resolution topography for advancing the understanding of mass and energy transfer through landscapes: A review, *Earth-  
Science Rev.*, 148, 174–193, <https://doi.org/10.1016/J.EARSCIREV.2015.05.012>, 2015.

1140 Pavlis, T. L. and Bruhn, R. L.: Application of LIDAR to resolving bedrock structure in areas of poor exposure: An example  
from the STEEP study area, southern Alaska, *GSA Bull.*, 123, 206–217, <https://doi.org/10.1130/B30132.1>, 2011.

~~Phillips, J. D.: Divergence, Convergence, and Self Organization in Landscapes, 89, 466–488, [https://doi.org/10.1111/0004-  
5608.00158](https://doi.org/10.1111/0004-5608.00158), 2010.~~ Pirotti, F. and Tarolli, P.: Suitability of LiDAR point density and derived landform curvature maps for  
channel network extraction, *Hydrol. Process.*, 24, 1187–1197, <https://doi.org/10.1002/HYP.7582>, 2010.

1150 Prakash, N., Manconi, A., and Loew, S.: Mapping Landslides on EO Data: Performance of ~~Deep Learning Models vs.  
Traditional Machine Learning Models~~[deep learning models vs. traditional machine learning models](https://doi.org/10.3390/RS12030346), *Remote Sens.*, 12, 346,  
<https://doi.org/10.3390/RS12030346>, 2020.

Reed, S.: Merced, CA: Origin and evolution of the Mima mounds, National Center for Airborne Laser Mapping, distributed by OpenTopography [data set], <https://doi.org/10.5069/G93B5X3Q>, 2006.

1155 Reed, S. and Amundson, R.: Using LIDAR to model Mima mound evolution and regional energy balances in the Great Central Valley, California, *Spec. Pap. Geol. Soc. Am.*, 490, 21–41, [https://doi.org/10.1130/2012.2490\(01\)](https://doi.org/10.1130/2012.2490(01)), 2012.

van Rijsbergen, C. J.: *Foundation of evaluation*. *J. Doc.*, 30, 365-373, <https://doi.org/10.1108/eb026584>, 1974.

1160 Roering, J. J., Marshall, J., Booth, A. M., Mort, M., and Jin, Q.: Evidence for biotic controls on topography and soil production, *Earth Planet. Sci. Lett.*, 298, 183–190, <https://doi.org/10.1016/J.EPSL.2010.07.040>, 2010.

Roering, J. J., Mackey, B. H., Marshall, J. A., Sweeney, K. E., Deligne, N. I., Booth, A. M., Handwerger, A. L., and Cerovski-Darriau, C.: “You are HERE”: Connecting the dots with airborne lidar for geomorphic fieldwork, 200, 172–183,

1165 <https://doi.org/10.1016/j.geomorph.2013.04.009>, 2013.

Rossi, M. W., Anderson, R. S., Anderson, S. P., and Tucker, G. E.: Orographic Controls on Subdaily Rainfall Statistics and Flood Frequency in the Colorado Front Range, USA, *Geophys. Res. Lett.*, 47, e2019GL085086, <https://doi.org/10.1029/2019GL085086>, 2020.

1170

Sofia, G.: Combining geomorphometry, feature extraction techniques and Earth-surface processes research: The way forward, 355, 107055, <https://doi.org/10.1016/J.GEOMORPH.2020.107055>, 2020.

Sokolova, M. and Lapalme, G.: A systematic analysis of performance measures for classification tasks, *Inf. Process. Manag.*, 45, 427-437, <https://doi.org/10.1016/j.ipm.2009.03.002>, 2009.

1175

Tucker, G. E. and Hancock, G. R.: Modelling landscape evolution, *Earth Surf. Process. Landforms*, 35, 28–50, <https://doi.org/10.1002/ESP.1952>, 2010.

van Rijsbergen, C. J.: *Information Retrieval*, 1979.

1180

Wang, Y., Fang, Z., and Hong, H.: Comparison of convolutional neural networks for landslide susceptibility mapping in Yanshan County, China, *Sci. Total Environ.*, 666, 975–993, <https://doi.org/10.1016/J.SCITOTENV.2019.02.263>, 2019.

185 [Zheng, X. and Chen, T.: High spatial resolution remote sensing image segmentation based on the multiclassification model and the binary classification model, Neural Comput. Appl., 35, 3597–3604, <https://doi.org/10.1007/S00521-020-05561-8>, 2023.](https://doi.org/10.1007/S00521-020-05561-8)